Journal of Geosciences, 68 (2023), 3–24 DOI: 10.3190/jgeosci.365

Original paper

Eruptive and magmatic evolution of North Chamo Volcanic Field (southern Ethiopia)

Vladislav RAPPRICH[1]*, Vojtěch JANOUŠEK[1], Tomáš HROCH[1], Jitka MÍKOVÁ[1], Vojtěch ERBAN[1°], Firdawok LEGESA[2], Zoltán PÉCSKAY[3], Patricie HALODOVÁ[1°°]

[1] *Czech Geological Survey, Klárov 3, 118 21 Prague 1, Czech Republic; vladislav.rapprich@geology.cz*
[2] *Geological Survey of Ethiopia, Gurd Shola, P.O. Box 2302, Addis Ababa, Ethiopia*
[3] *Isotope Climatology & Environmental Research Centre (Icer) K–Ar Group, Institute for Nuclear Research (ATOMKI), Bem tér 18/c, 4026 Debrecen, Hungary*
**Corresponding author*
° *Actually at Pragolab Ltd., Nad Krocínkou 55, 190 00 Prague 9, Czech Republic*
°° *Actually at Department of Material and Mechanical Properties, Research Centre Řež, Hlavní 130 Řež, 250 68 Husinec, Czech Republic*

A group of pyroclastic cones is dispersed in the North Chamo Volcanic Field, i.e. in the northern surroundings of the Chamo Lake and over neighbouring part of the Nech Sar plains (southern termination of the Main Ethiopian Rift). The activity of scattered cinder cones was partly coeval with that of Tosa Sucha Volcano (Calabrian), but continued also after Tosa Sucha's extinction until Middle Pleistocene (*c.* 0.5 Ma). Whereas scoria cones on the Nech Sar plains displayed a rather simple Strombolian eruptive style, the cones located within the northern part of Chamo Lake were characterized by more complex evolution. Ganjulle scoria cone, with a uniform olivine basalt composition, started with a Surtseyan-style eruption, which turned into Strombolian as the volcano grew above the water level. An even more complex history was documented for the Ganta cone. Compositional zoning of pyroclastic rocks is explained by zoned-chamber exhaustion. The transition from magmatic to phreatomagmatic style of the eruption was then most likely linked to syn-eruptive subsidence of the area on the Chamo Lake banks. Subsequent transition back to Strombolian style reflected the growth of the cone above water level.

The Sr–Nd–Pb isotopes, together with major-element-based thermodynamic modelling, demonstrate that magmas parental to the North Chamo alkaline volcanic rocks (alkali basalt, through trachybasalt and trachyandesite to trachyte) evolved initially by closed-system fractionation of olivine, later joined by clinopyroxene, spinel and calcic plagioclase. The subsequent stage was characterized by a substantial (*c.* 25% by mass) assimilation of country-rock felsic igneous material, perhaps corresponding to the Paleogene ignimbrites.

Keywords: magma fractionation, mineral chemistry, Sr–Nd–Pb isotopes, K–Ar geochronology, North Chamo Volcanic Field, Main Ethiopian Rift
Received: 4 April 2022; accepted: 30 November 2022; handling editor: V. Kachlík
The online version of this article (doi: 10.3190/jgeosci.365) contains electronic supplementary material.

1. Introduction

Main Ethiopian Rift (MER) represents a continental rift in its mature phase, which is associated with almost strictly bimodal volcanism (e.g., Gasparon et al. 1993; Biggs et al. 2021). The erupted magmas comprise primitive, basic and highly silicic types, respectively. Eruptions of basic and silicic magmas alternated periodically during rift-opening as well as during mature-rift stages. The silicic rocks, mainly alkaline rhyolites, have been emitted from large central volcanoes (e.g., Rapprich et al. 2016; Martin-Jones et al. 2017; Fontijn et al. 2018), but form also wide-spread ignimbrite sheets. Mafic primitive lavas, forming in previous periods extensive lava sheets, erupted since Late Pleistocene till Holocene mostly from monogenetic volcanoes, usually arranged in elongated volcanic fields following rift-faults (e.g., Rooney 2010; Rooney et al. 2011; Megerssa et al. 2019; Hunt et al. 2020).

Intermediate rocks, on the other hand, occur only scarcely. Fissures emitting lavas of intermediate composition are associated with Boset-Bericha Volcanic Complex in the central MER (350 km NE of study area; Siegburg et al. 2018), whereas accidental occurrences of intermediate rocks in other complexes are mostly of hybrid origin. From this point of view, the southern termination of the Main Ethiopian Rift, namely the area of Tosa Sucha, Chamo Lake and Nech Sar plains offers a unique opportunity to study petrogenesis of intermediate volcanic rocks. Results of such research may shed new light on the genetic relationships between rift-floor basalts and alkaline rhyolites of the Main Ethiopian Rift

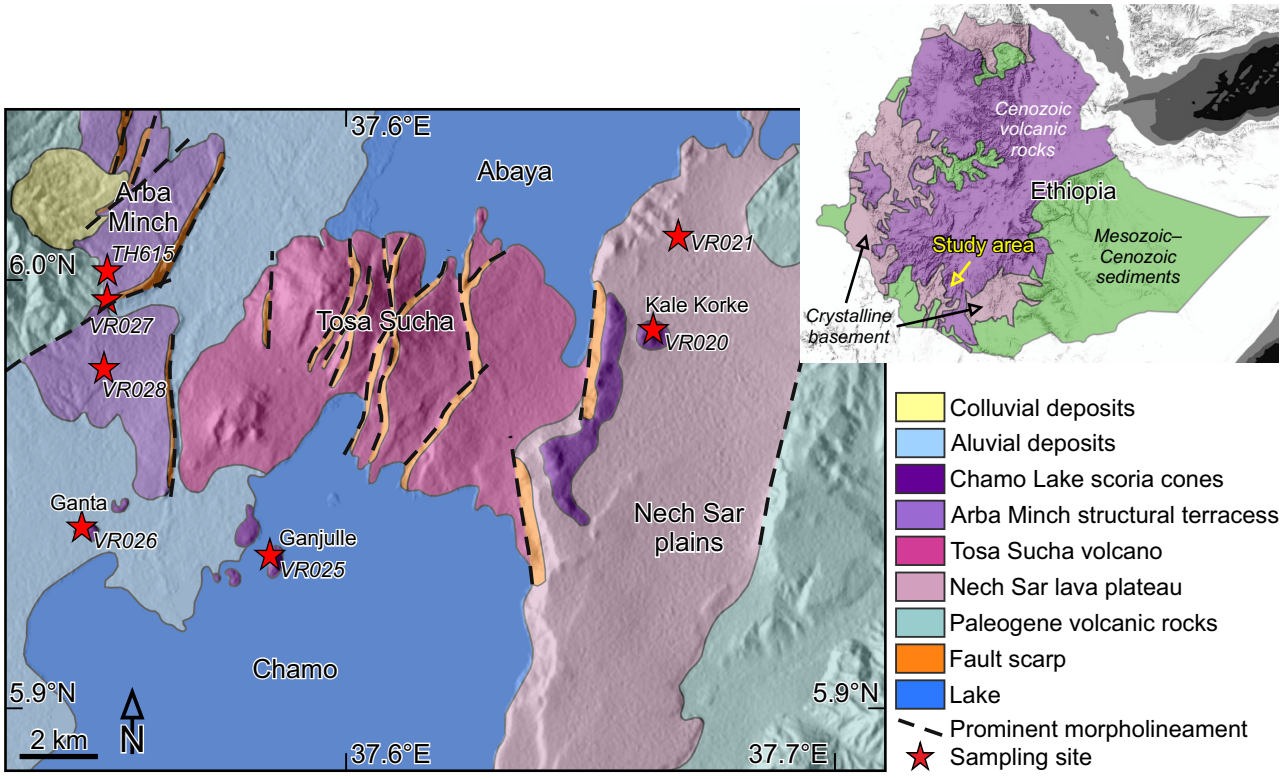

Fig. 1 Simplified geological sketch map of the study area; its location within the Main Ethiopian Rift is shown in the inset map. Positions of sampling points and discussed outcrops are also indicated.

as both compositionally contrasting groups may share similar radiogenic isotope signatures (e.g., Trua et al. 1999; Peccerillo et al. 2003; Rapprich et al. 2016).

Our investigation therefore focused on eruptive history, petrology and petrogenetic model for Pleistocene volcanic rocks erupted from scattered pyroclastic cones in the area of Arba Minch, Nech Sar and northern Chamo Lake with an aim to better understand petrogenesis of intermediate rocks in the MER and, in particular, tectono-volcanic evolution of the southern MER termination.

2. Geological setting

Prior to the onset of rifting, the Ethiopian shield experienced voluminous trap-basalt effusions during rather short period (less than 1 M.y.) in Early Oligocene (e.g., Rochette et al. 1998; Ayalew et al. 2021). Subsequently, the MER started to open, propagating from north southwards, being associated with voluminous bimodal alkaline volcanism (e.g., Corti 2009; Biggs et al. 2021). The most developed section of the rift is represented by its transition to MORB-producing ocean-spreading centre in the northerly Afar region (e.g., Barrat et al. 2003). Individual evolutionary stages in different parts of the MER were not synchronous, and their transition in time was also rather gradual.

North Chamo Volcanic Field is located in the southern part of the MER, i.e. in its youngest segment where the rift width decreases to some 30 km from the original *c.* 80–100 km. The metamorphic basement of the Arabian–Nubian Shield is covered here by Paleogene basaltic lavas intercalated with welded to unwelded rhyolitic ignimbrites associated with minor pyroclastic fall deposits (Verner et al. 2018). These earlier volcanic sequences – formed during pre-rift traps and by repeated voluminous eruptions related to gradual and multi-stage rift opening – are crosscut by rift-bounding faults and are exposed in the rift scarps. The rift floor consists of basaltic lavas forming structural terraces on both sides of the rift, i.e. Nech Sar plains and Arba Minch terraces (Fig. 1).

⇨

Fig. 2 Volcanic landforms and pyroclastic deposits. **a** – Faulted edifice of the Tosa Sucha Volcano viewed from Chamo Lake, remnants of younger scoria cones in the front. **b** – Nech Sar plains with erosional remnant of Alakom scoria cones. **c** – Kale Korke basaltic scoria cone on the Nech Sar plains. **d** – Ganjulle scoria cone in the northern part of Chamo Lake. **e** – Eruptive sequence of the Ganjulle scoria cone: phreatomagmatic lapilli deposits (P) crosscut by a system of feeding dykes (F) and overlain by scoriae from subsequent Strombolian phase eruption (S1); second Strombolian event (S2) followed after short break as indicated by weathering surface (w). **f** – Pyroclastic sequence of the Ganta scoria cone exposed in the temporary quarry: trachytic pumice (T) overlain by trachyandesitic phreatomagmatic deposits (TA-p) and the sequence is capped with trachyandesitic scoriae (TA-s), separated from TA-p layer by weathering surface (w).

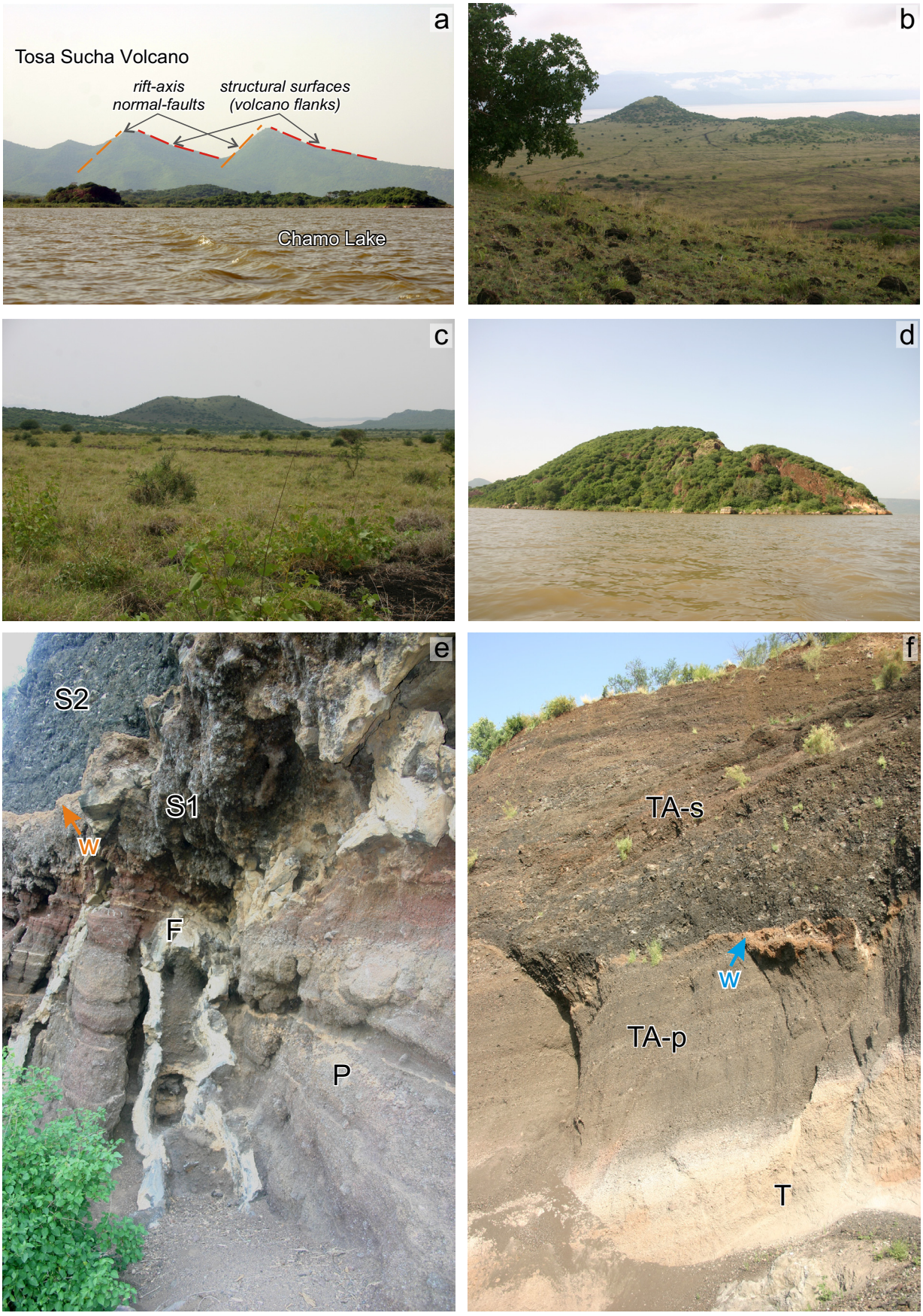
a
Tosa Sucha Volcano
rift-axis
normal-faults
structural surfaces
(volcano flanks)
Chamo Lake
b
c
d
e
S2
S1
W
F
P
f
TA-s
W
TA-p
T

Petrology of volcanic rocks building up the Arba Minch terraces, comprising rhyolitic ignimbrites and basalt to basaltic trachyandesite lavas, has been outlined by Berhanu (2019). The space between both parts of the rifted basaltic lava sheets is occupied by Abaya and Chamo lakes, separated from each other by the Pleistocene Tosa Sucha Volcano (George and Rogers 1999). The Tosa Sucha Volcano has been affected by the latest stages of rifting (Fig. 2a).

Several smaller scoria cones post-dating the faulting of the Tosa Sucha Volcano, scattered in the northern Chamo Lake and in the Nech Sar plains, are subject of this study. In some publications, the name 'Tosa Sucha' has also been adopted for the scattered monogenetic volcanoes in the vicinity, grouped together into a single lithostratigraphic unit. In this contribution, we distinguish the Tosa Sucha basaltic shield volcano proper from younger-appearing monogenetic cones with more variable composition herewith termed 'North Chamo Volcanic Field'.

3. Methods

3.1. Geomorphology and field work

The field campaign, carried out in 2012, comprised detailed description of pyroclastic sequences at available exposures and a collection of samples for further analytical work. The samples for petrographic description as well as for whole-rock and mineral chemistry analyses came either from coherent lavas and feeder-dykes or from larger juvenile bombs within pyroclastic deposits. The field observations and their extrapolations were supported by geomorphological interpretation of a multidirectional shaded relief extracted from SRTM Digital Elevation Model and satellite optical data of the World Imagery. The geomorphological data helped to identify individual volcanic landforms and specify the tectono-volcanic evolution of the study area.

3.2. Petrography and mineral chemistry

Thin sections were studied under a standard petrographic microscope. The quantitative chemical analyses of individual minerals were conducted on Tescan MIRA 3GMU electron microprobe housed at the laboratories of the Czech Geological Survey, Prague (CGS), fitted with SDD X-Max 80 mm^2 EDS detector and driven by AZtecEnergy software (Oxford Instruments). Point analyses of rock-forming minerals were acquired using 15 kV accelerating voltage, 15 mm working distance, 3 nA probe current, 30 s acquisition time and beam diameter of 30 nm. Mineral set of standards (SPI) was used for standardization, pure Co for quant optimization. The method of Vieten and Hamm (1978) balancing the deficiency of oxygen atoms corresponding to 4 cations (with all iron as Fe^{2+}) was employed for the calculation of Fe^{3+} contents in clinopyroxenes. The same method based on 3 or 13 cations (excluding Ca–alkali position) was applied also for opaque minerals and amphiboles, respectively.

3.3. Whole-rock chemistry

The collected samples were crushed in steel jaw crusher and pulverized in agate mill. Major-element analyses were carried out in the CGS. The analytical methods included atomic absorption spectrometry, photometry and titration with Complexon III, following the methodology described in Dempírová et al. (2010). The samples were dissolved in the first step using $HF + HNO_3 + H_2SO_4$ at 220 °C (determination of SiO_2), and in the second step in a $HCl + H_2SO_4$ mixture (remaining oxides).

The trace-element concentrations (Ba, Cr, Ga, Hf, Nb, Ni, Rb, Sr, V, Th, U, Zr, Y, REE) have been measured using a Thermo Fisher Scientific X Series II inductively coupled plasma mass spectrometer (ICP-MS), housed at the CGS. The sample decomposition involved an initial digestion by $HF–HClO_4$ mixture, followed by fusion of dried condensate in a Pt-beaker with $Li_2B_4O_7–Na_2CO_3$ mixture and finally leaching in 2% HNO_3.

Both whole-rock and mineral chemistry analytical data were visualized using the *GCDkit* software (Janoušek et al. 2006).

3.4. K–Ar geochronology

Five samples of lavas and volcanic bombs from the North Chamo Volcanic Field were dated using the potassium–argon method in the ATOMKI K–Ar Laboratories (Debrecen, Hungary). For potassium determination, approximately 0.05 g of finely ground samples were digested in acids (HF, HNO_3) in Teflon beakers and finally dissolved in 0.2 M HCl. Potassium was determined by flame photometry with a Na buffer and Li internal standard using Industrial M420 type flame photometer. Multiple runs of inter-laboratory standards (Asia1/95, LP-6, HD-B1, GL-0) indicated the accuracy and reproducibility of this method to be within 2 %.

For Ar measurements, *c.* 0.5 g samples were wrapped in aluminium foil and copper sieve preheated for about 24 h at 150–180 °C in vacuum. Argon was extracted under ultra-high vacuum conditions by RF induction heating and fusion of rock samples in Mo crucibles. The gas was purified by Ti sponge and SAES St 707 type getters (to remove chemically active gas contaminants) and liquid-nitrogen filled cold trap (to remove condensable gases).

The extraction line is linked directly to a mass spectrometer (90° magnetic sector type of 155 mm radius,

equipped with a Faraday cup, built in ATOMKI, Debrecen, Hungary) and the analyses were carried out in static mode. Argon isotope ratios were measured by an ^{38}Ar isotope dilution mass spectrometric method, previously calibrated with atmospheric argon and international rock standards. Experimental details of the K–Ar dating method used at ATOMKI Debrecen and results of calibration have been described in Balogh (1985). Age of the samples is calculated using the decay constants suggested by Steiger and Jäger (1977). Analytical errors are given at 68 % confidence level (1σ).

3.5. Radiogenic isotopes

Selected samples were analyzed for Sr–Nd–Pb isotopic ratios. Entire leaching and chemical separation procedures were carried out in Class 10,000 clean lab and the mass spectrometric analyses were performed at the CGS. Sample handling in lab was carried out in Class 100 laminar flow hoods. All reagents used for Sr and Nd separation were in-house double distilled acids (in DST-1000, Savillex); for Pb leaching, dissolution and separation UpA quality Romil acids were used. All dilutions were made using milliQ water, and all labware was acid-washed prior to use. All samples were dissolved using an acid digestion in a closed vessel using a 3 : 7 mixture of concentrated HNO_3 and HF acids on a hotplate at 180 ºC for ~72 h. Afterwards, the dissolved samples were evaporated, 3 ml of HNO_3 were added to the residues, dried three times, and finally re-digested in 8 ml of 6M HCl. Samples for Pb were digested separately from those for Sr–Nd isotopic determinations.

The Sr–Nd analytical procedure consists of triple column ion exchange chemistry. Strontium and REE were isolated from the bulk matrix by following the ion-exchange chromatography techniques of Pin et al. (1994) (PP columns filled with Sr.Spec and TRU.Spec Eichrom resins for separation of Sr and bulk REE, respectively). The Nd was further separated from the REE fraction on PP columns with Ln.Spec Eichrom resin; further analytical details were reported by Míková and Denková (2007).

The Sr–Nd isotopic analyses were performed on a Thermo Finnigan Neptune multi-collector (MC) ICP-MS. The measured Sr isotopic ratios were corrected for mass-dependent instrumental fractionation using exponential law and assuming $^{86}Sr/^{88}Sr = 0.1194$ (Steiger and Jäger 1977). The isobaric interference of Rb at the mass 87 was corrected, if necessary, using a natural value of $^{87}Rb/^{85}Rb = 0.3857$ (Steiger and Jäger 1977). Reproducibility of the isotopic determinations is estimated form replicate analyses of the NIST NBS 987 reference material during analytical session, with an average $^{86}Sr/^{88}Sr = 0.710338 \pm 10$ (2σ), n = 8.

The measured $^{143}Nd/^{144}Nd$ ratios were corrected for mass-dependent instrumental fractionation using exponential law to $^{146}Nd/^{144}Nd = 0.7219$ (Wasserburg et al. 1981). If present, the isobaric interference of Sm at mass 147 was corrected assuming natural isotopic ratio of $^{144}Sm/^{147}Sm = 0.20648$. During analytical session the replicate analyses of Nd reference material JNdi-1 (Tanaka et al. 2000) gave external reproducibility with an average $^{143}Nd/^{144}Nd = 0.512114 \pm 12$ (2σ), n = 8.

Acid leaching of sample powders prior to dissolution and Pb isotopic analysis has been employed to remove all secondary material (Bouvier et al. 2005; Nobre Silva et al. 2009). The acid-leaching procedure followed that of A. Stracke (personal communication). Approximately 0.1–0.6 g of sample chips was acid-leached with 14 ml of 6M HCl in a Savillex beaker in an ultrasonic bath for 60 min. The supernatant was immediately decanted; the samples were flushed and decanted twice with milliQ water and then acid digested. Subsamples of digested material were analysed for Pb concentration after the acid-leaching procedure.

In preparation for Pb chromatographic separation, the samples were dried and redissolved in 2M HCl and loaded onto a pre-cleaned and conditioned 0.2 ml column packed with Sr.Spec resin (50–100 mesh; Triskem, France). The matrix was washed out with 2M HCl and thereafter Pb was eluted in 6M HCl, leading to ~100% recovery of Pb. After chemical purification, the eluted Pb fraction was dried, a small quantity of concentrated HNO_3 was added to remove any organic material eluted from the resin along with the Pb, and it was dried again. Finally, the dried Pb fractions were redissolved in 1 ml of 2% HNO_3 with Tl spike and left overnight to homogenize on a hot plate.

The Pb isotopic analyses were performed on a Neptune MC-ICP-MS (Thermo Scientific). Instrumental mass fractionation was monitored and corrected online using a NIST SRM 997 Tl standard solution; potential ^{204}Hg isobaric interference on ^{204}Pb was monitored at mass ^{202}Hg and corrected by assuming natural Hg isotopic abundances ($^{202}Hg/^{204}Hg = 4.35$). Sample analysis followed a sample–standard bracketing protocol in which the SRM-981 Pb standard was run after every sample. The results were then normalized off-line to the SRM-981 certified values and combined statistics for three repeated measurements were calculated.

3.6. Thermodynamic modelling

The major-element based thermodynamic modelling of magma evolution during energy-constrained assimilation and fraction crystallization (AFC; i.e. no recharge) has been performed by the PhaseEQ module of the Magma Chamber Simulator (aka MCS, June 2021 release;

https://mcs.geol.ucsb.edu) (Bohrson et al. 2014, 2020). The calculations utilized the rhyolite-MELTS + H_2O–CO_2 fluid (Melts-batch-v1.2.0) thermodynamic engine (Ghiorso and Sack 1995; Gualda et al. 2012; Ghiorso and Gualda 2015).

The simulations, whose results are reported in this study, were isobaric, assuming relatively shallow conditions (1 kbar). Temperature decrement step for fractional crystallization was set to 10 °C; the initial rock to wall-rock ratio to 1 : 1.5. The starting wall-rock temperature was assumed to be 500 °C. The oxygen fugacity was maintained at the fayalite–magnetite–quartz (FMQ) buffer and thus the magma–wall-rock system was considered opened with respect to oxygen. The composition of the primitive melt was approximated by the sample VR025, but its original H_2O content was prescribed to 2 wt. % and CO_2 set to zero. The presumed assimilant had composition of ignimbrite TH615. For further settings (the MES file) and complete spreadsheet with the MCS modelling output, see the Electronic Supplementary Material (ESM).

4. Results

4.1. Tectono-volcanic evolution of the area

Although the previous studies used to merge all Plio–Pleistocene volcanic rocks of this area into a single lithostratigraphic unit, the field data complemented with interpretation of geomorphology allowed us to subdivide these rock sequences into several stages (Fig. 1):

1) The oldest activity produced basaltic lavas forming widespread plateaux of structural terraces east of Chamo and Abaya lakes with remnants of eroded scoria cones.
2) The second phase was characterized by the growth of Tosa Sucha (God's bridge) Volcano, which forms a barrier separating Abaya and Chamo lakes. The morphology of Tosa Sucha features gentle back-slopes of preserved volcano flanks separated by steep front-slopes representing scarps of SSW–NNE-trending normal faults (Fig. 2a).
3) The youngest, third phase corresponded to the formation of morphologically well-preserved pyroclastic cones and pyroclastic ring scattered over northern part of the Chamo Lake. Moreover, the sequences of basaltic lavas with alluvial gravel intercalations build up structural terraces west of Tosa Sucha Volcano (Arba Minch terraces).

4.2. Volcanic landforms and pyroclastic deposits

North Chamo Volcanic Field comprises several scoria cones, with morphology variably modified by subsequent tectonic activity, erosion or quarrying. Although some of the cones of this volcanic field were probably active already synchronously with the Tosa Sucha Volcano (2.5–0.7 Ma: George and Rogers 1999), several of them post-dated the rift-related structures cross-cutting the Tosa Sucha Volcano (Fig. 2a) and the scoria cones are commonly located on the morphologically evident fault-scarps.

Probably the oldest cone of the entire field is the **Alakom Hill** (VR021; Fig. 2b) on the Nech Sar plains. The pyroclastic facies of this volcano was completely removed by erosion and solely the feeding neck of olivine basalt remains.

Kale Korke scoria cone (VR020) rising above basaltic plain of Nech Sar has morphologically well-preserved shape with an asymmetric crater open towards south (Fig. 2c). The cone consists of unconsolidated accumulation of basaltic scoriae (clasts 3–10 cm across) with frequent spindle-shaped bombs up to 50 cm long.

Ganjulle scoria cone rising from the Chamo Lake (VR025; Fig. 2d) has already been affected by erosion and/or by faulting; therefore, its original crater is not preserved. According to its morphology, the entire island most likely represents only eastern part of the original pyroclastic cone. The exposed pyroclastic sequence consists of three layers (Fig. 2e). The lowermost, ill-sorted clast-supported non-welded layer (layer P in Fig. 2e) is slightly bedded with individual beds of massive texture and thickness in the range of 20–40 cm. These uncompacted deposits are dominated by non-vesiculated basaltic lapilli (mostly 1–2 cm, occasionally up to 6 cm). Feeding dykes (F) penetrating the lapilli deposits (P) are connected with partly welded agglomerates (scoria breccia – S1), covering the lapilli beds. Surface of the agglomerates (S1) was subject to fossil weathering (w), suggesting break in volcanic activity. The subsequent deposits consist of clast-supported ill-sorted black basaltic scoriae (S2) with massive texture and absence of bedding. Two nameless crescent-shaped islets located about 1 km west of Ganjulle appear to be remnants of another tuff ring. Remnants of this tuff ring were not accessed and any interpretation of this volcanic feature rely on aerial photos only.

Small quarry on the Chamo Lake banks near the road from Arba Minch to Konso exposes pyroclastic sequence of **Ganta cone** (samples VR026; Fig. 2f). The lower portion of this sequence consists of trachytic pumice (T) with trachytic lava (sample VR026D) exposed in the lowermost part, in a small trough. The boundary between trachytic lava and trachytic pumice is not well exposed. The lava probably formed only smaller tongue within the pyroclastic deposits, with foamy and brecciated surface texturally very similar to ill-sorted near-vent pumice fall. This fact – together with limited exposure – contributes to the obscured boundary between both lithologies. The pumice deposit is generally ill-sorted, clast-supported and massive. Larger pumice fragments may reach 30 cm in diameter. Upwards, the pumice passes gradually into

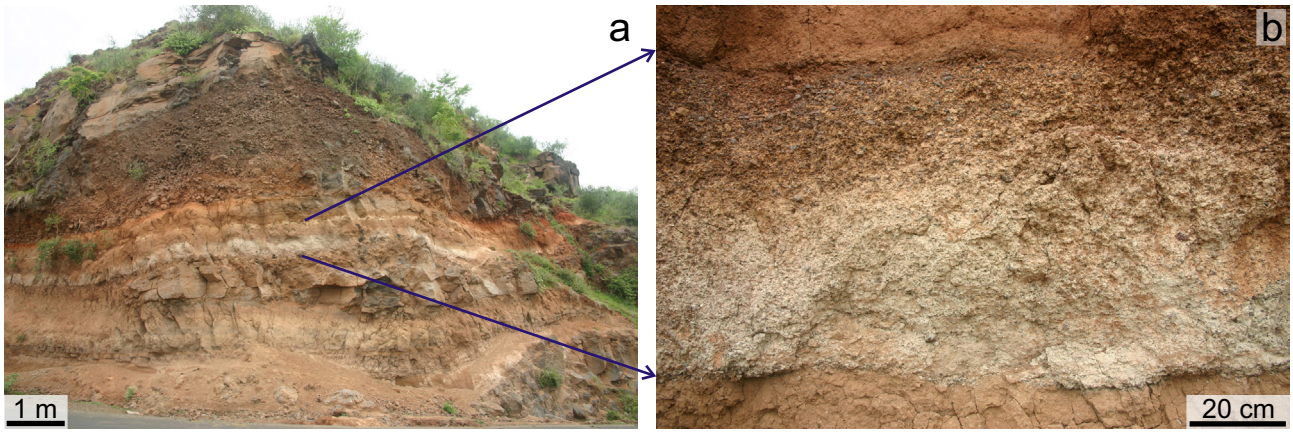

Fig. 3 Characteristic compositionally zoned distal pyroclastic fall deposit from the Ganta scoria cone deposit exposed in the road-cut on the southern limit of Arba Minch.

darker deposit (Fig. 2f). This darker layer (TA-p; sample VR026B) is bedded, locally with signs of diagonal bedding. It is ill-sorted, clast-supported and consists of non-vesiculated angular fragments of trachyandesite. The most abundant grain size varies around 1 cm, but the clasts may reach up to 20 cm. Surface of this trachyandesite lapilli-dominated deposit is irregular with thin layer of weathering products (w). The sequence is then capped with thick accumulation of moderately sorted, clast-supported trachyandesite scoriae with frequent irregular bombs up to 50 cm in diameter (TA-s; sample VR026C).

A pyroclastic layer with well visible transition from trachytic pumice-dominated zone to trachyandesite lava fragments-dominated one was documented also in the road-cut of the serpentine on the southern limit of Arba Minch (Fig. 3). The unique texture of this pyroclastic layer, with characteristic gradual transition from pumice-dominated bottom to trachyandesite lithic-dominated top, allows us to link this layer with the Ganta scoria cone. This bicolour layer is sandwiched between trachyandesitic lava flows (Fig. 3a) and reaches 60 cm thickness on the southern edge of the Arba Minch. This layer rapidly thins out northwards; on the cliffs built by the same trachyandesitic lavas more to the north (Arba Minch University campus) it does not occur anymore.

4.3. Petrography

The studied rocks span from olivine basalt, trachybasalt and trachyandesite to trachyte.

Olivine basalt – was sampled as coherent lava bomb from the Kale Korke scoria cone (sample VR020) and as a feeder-dyke in the Ganjulle cone (sample VR025). The porphyritic dark-grey rock contains frequent randomly oriented euhedral phenocrysts of olivine and clinopyroxene (both around 0.5 mm, occasionally up to 1 mm; Fig. 4a–b). Phenocrysts of plagioclase occur more scarcely and do not exceed 0.5 mm (mostly under 0.3 mm). The phenocrysts are enclosed in dark (oxidized) groundmass, containing microcrysts of clinopyroxene, olivine, plagioclase and opaque minerals.

Trachybasalt – is present in the form of volcanic neck exposed by selective erosion from pyroclastic cone on Alakom Hill (VR021). The finely porphyritic dark-grey rock contains sparse phenocrysts of olivine and clinopyroxene (both 0.3–0.7 mm) enclosed in fine-grained matrix dominated by plagioclase laths, abundant magnetite and less frequent clinopyroxene microcrysts.

Trachyandesite – was sampled as coherent lava fragments in phreatomagmatic layer, a juvenile bomb in Strombolian layer of Ganta cone (samples VR026B and VR026C, respectively) and from a lava south of Arba Minch (sample VR028). Despite the fact that they represent different types of pyroclastic deposits of distinct age, i.e. a lava clast of phreatomagmatic phase (VR026B) vs. a juvenile bomb of Strombolian phase (VR026C), both rocks display identical petrography. The greyish rock has trachytic texture. Abundant euhedral plagioclase phenocrysts (up to 0.3 mm) and scarcer euhedral clinopyroxene phenocrysts (up to 0.2 mm) are enclosed in groundmass of plagioclase, magnetite and pale-brown isotropic glass (Fig. 4c–d). The general trend of preferred orientation is the same for phenocrysts as for the groundmass.

Trachyte – is represented by a sample of lava from Ganta scoria cone (sample VR026D). The light-grey rock is fine-grained and aphyric with scarce microcrysts of clinopyroxene, amphibole and magnetite (not exceeding 0.1 mm) surrounded by prevailing feldspar laths (0.1–0.2 mm). Shape-preferred orientation of feldspars is adopted also by clinopyroxene and amphibole (Fig. 4e–f).

4.4. Mineral chemistry

Olivine, which is present in olivine basalts but also in trachyandesite VR026C, displays wide compositional variation in the studied rocks (ESM 1). The most mag-

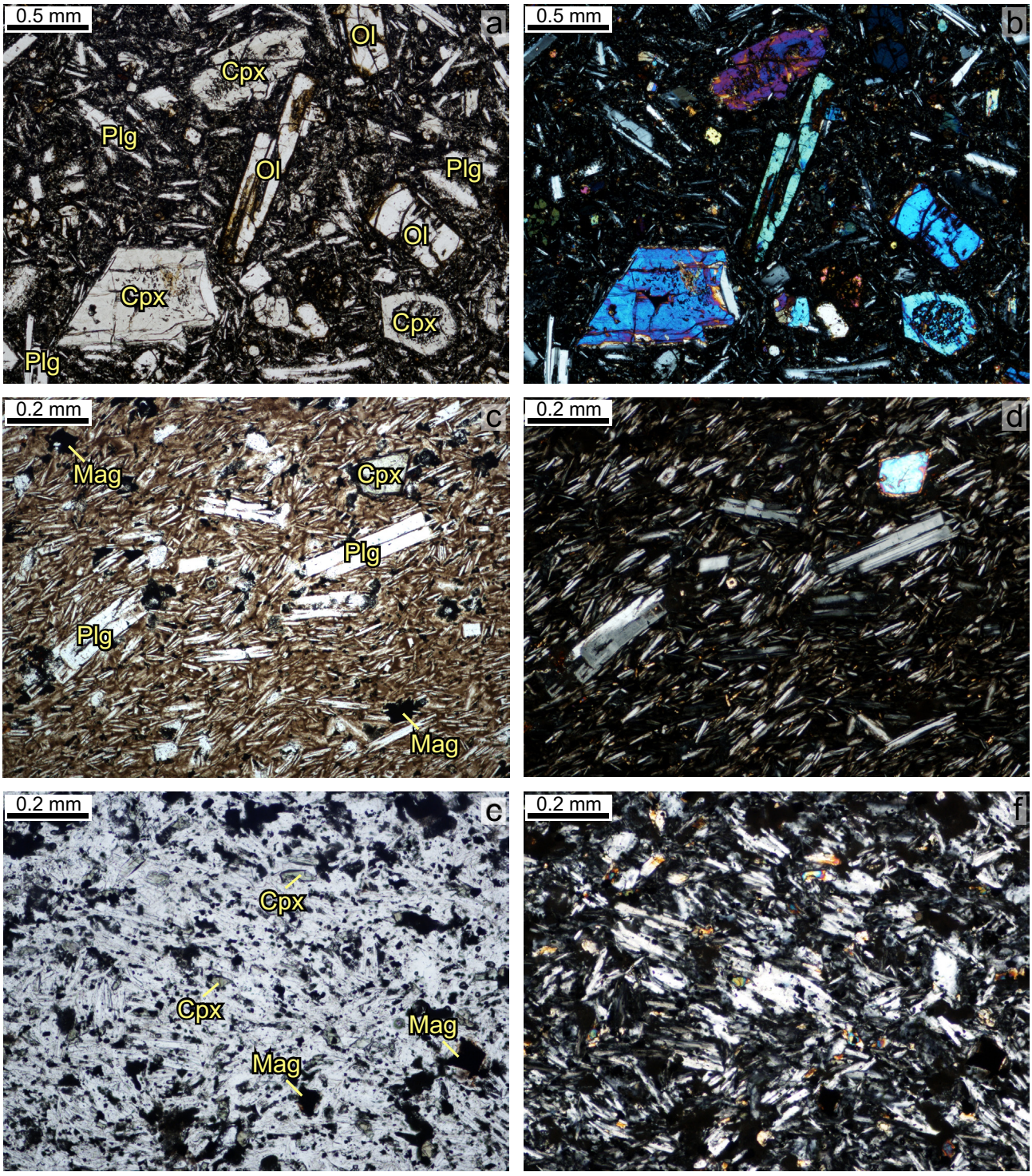

Fig. 4 Photomicrographs of representative rock-samples (a, c, e – plane-polarized light; b, d, f – cross-polarized light). **a–b** – Olivine basalt from Ganjulle (sample VR025). **c–d** – Trachyandesite from Ganta – larger lava shred (sample VR026B). **e–f** – Trachyte from Ganta lava fragment of pumice deposit (sample VR026D). Cpx – clinopyroxene, Mag – magnetite, Plg – plagioclase, Ol – olivine.

nesian compositions form cores of larger phenocrysts in olivine basalts (Fo up to 86 in VR025, and up to 89 in the sample VR020). The rimward decrease in Mg is more significant in the sample VR025, where the rims and groundmass microcrysts have composition of $Fo_{43–58}$. The olivine evolution in the basalt VR020 stopped at $Fo_{80–82}$, while groundmass microcrysts may be slightly more ferrous ($Fo_{79–81}$).

Clinopyroxene is present in all investigated rock samples (ESM 2). Despite plotting along the augite/

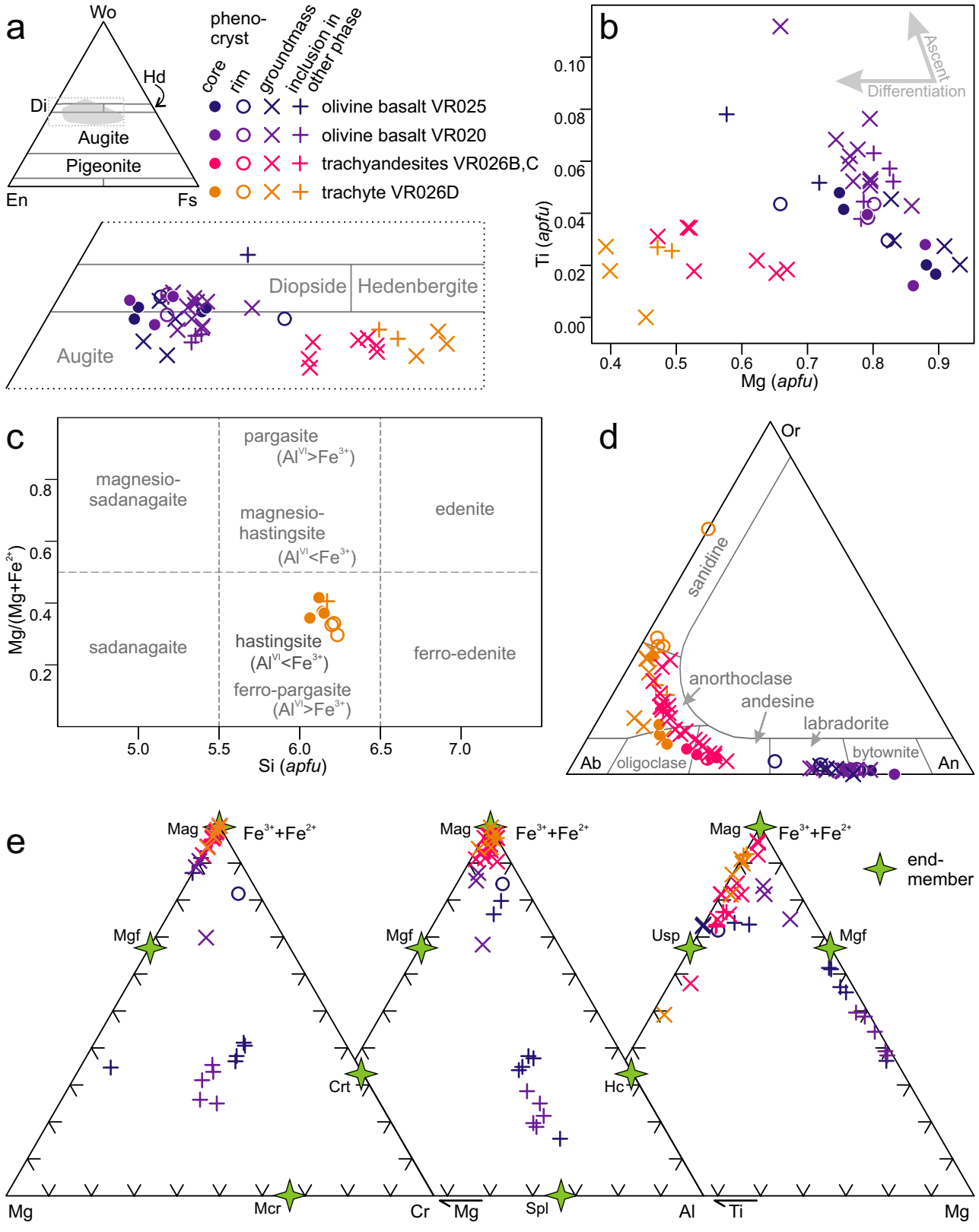

Fig. 5 Mineral chemistry. **a** – Quadrilateral classification diagram of pyroxenes (after Morimoto 1988). **b** – Ti (*apfu*) vs. Mg (*apfu*) binary diagram for studied clinopyroxenes. **c** –Classification of amphiboles from the trachyte (Leake et al. 1997). **d** – Classification of feldspars. **e** – Composition of analysed opaque phases displayed in Mg–Fe_{tot}–Cr, Mg–Fe_{tot}–Al and Ti–Fe_{tot}–Mg ternary diagrams.

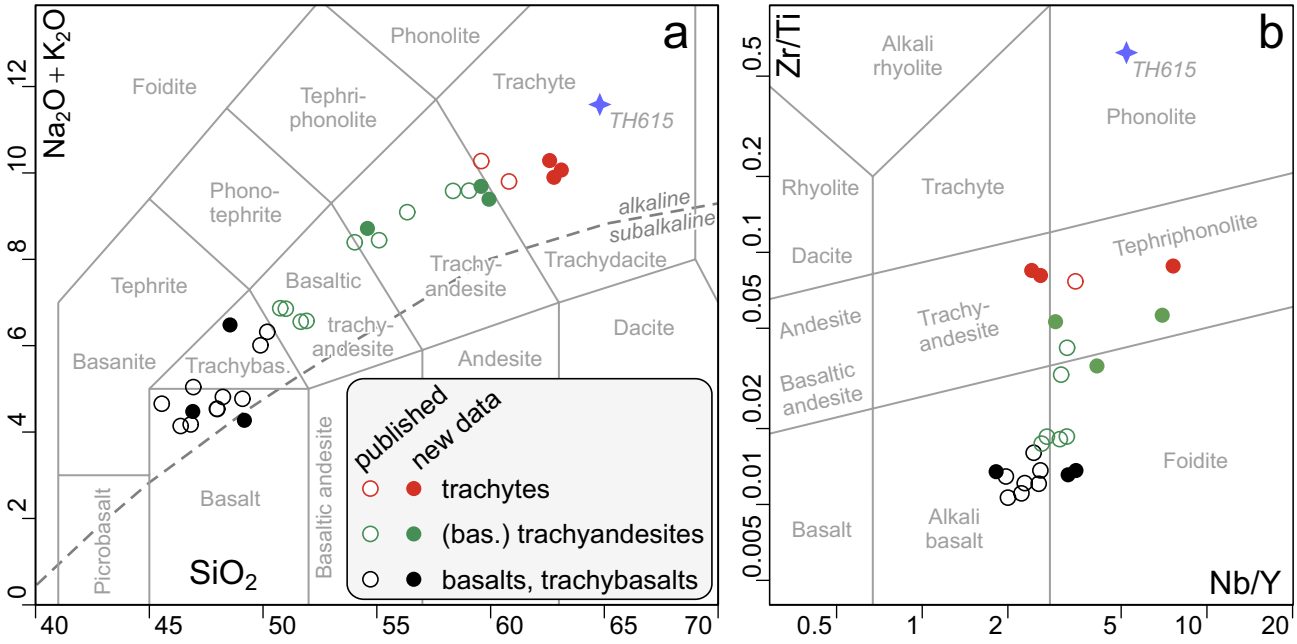

Fig. 6 Bulk-rock classification diagrams: **a** – TAS diagram (Le Maitre et al. 2002); **b** – Zr/Ti vs. Nb/Y discrimination diagram (Pearce 1996). Published data from George and Rogers (1999) and Rooney (2010).

diopside boundary in the classification diagram (Fig. 5a; Morimoto 1988), their Ca content not exceeding 0.9 *apfu* points to a common augite character of all analysed crystals. Significant shift towards more ferrous composition of augite follows the magma differentiation trend from olivine basalt to trachyte (Fig. 5a). When Mg (*apfu*) content as a proxy of differentiation is plotted against Ti (*apfu*) reflecting decreasing pressure (e.g., Tracy and Robinson 1977; Rapprich et al. 2017), two different trends can be observed (Fig. 5b). Increasing Ti content towards the phenocrysts' rims and groundmass microcrysts in olivine basalt samples suggests that the clinopyroxene crystallization continued during magma ascent until the eruption. Stable Ti with decreasing Mg contents in clinopyroxene from trachyandesites and trachyte, on the other hand, imply crystallization of this mineral solely in the magma chamber, prior to the eruption onto surface.

Amphibole accompanies the clinopyroxene in the groundmass of trachyte VR026D (ESM 3). All analysed amphiboles are classified as hastingsite (Fig. 5c; Leake et al. 1997) with slight decrease in Mg and increase in Si from groundmass microcryst cores towards the rims.

Feldspars form two main compositional clusters (Fig. 5d; ESM 4). Calcic plagioclase (bytownite to labradorite) crystallized in olivine basalts. Bytownite forms mainly phenocryst cores, less so groundmass microcrysts, whereas most groundmass microcrysts and phenocryst rims consist of labradorite. Considerable compositional variability is seen in trachyandesites, where feldspars span from andesine to anorthoclase fields. The trachyte as the most evolved rock is dominated by anorthoclase groundmass enclosing phenocrysts of oligoclase mantled by anorthoclase to sanidine rims.

Opaque phases are various spinel-group minerals (Fig. 5e; ESM 5). We do not refer to opaques as to magnetite due to their very complex mineralogy. The smaller inclusions in olivine and clinopyroxene of olivine basalts are dominated by spinel and chromite/magnesiochromite components, and these constituents remain present in significant amounts also in later crystallized grains, of rather magnesioferrite character. The last stage of opaque's crystallization, found in all analysed rocks, corresponds to magnetite–ulvöspinel solid solution with variable proportions of both end-members (Fig. 5e).

4.5. Bulk-rock geochemistry

The whole-rock compositional data for analysed rocks (see Tab. 1), together with published data from Tosa Sucha Volcano and surrounding monogenetic cones (George and Rogers 1999; Rooney 2010), form a single common trend in the TAS diagram (Le Maitre et al. 2002) extending from alkali basalt, through trachybasalt and (basaltic) trachyandesite to trachyte (Fig. 6a). This trend (alkali basalt–trachyandesite–trachyte) is mimicked also in the Zr/Ti vs. Nb/Y diagram, i.e. a proxy to the standard TAS plot using less mobile elements (Pearce 1996; Fig. 6b). However, some analyses show elevated Nb/Y ratios (alkalinity proxy), most likely due to overestimated Nb contents.

In the chondrite-normalized spider plot (Boynton 1984; Fig. 7a), the analysed rocks form two groups, sepa-

Tab. 1 Major-element (in wt. %) and trace-element (in ppm) data for analysed rocks

Sample	VR020	VR021	VR025	VR026A	VR026C	VR026C2	VR026D	VR026D2	VR028	TH615
Rock	olivine basalt bomb	trachybasalt	olivine basalt	trachyte pumice	trachy-andesite bomb	trachy-andesite bomb (repeated sample)	trachyte	trachyte (repeated sample)	trachy-andesite	ignimbrite
SiO_2	48.01	47.42	46.23	62.19	58.33	58.72	62.14	61.59	54.00	63.40
TiO_2	1.61	2.24	1.46	0.56	0.83	0.81	0.62	0.60	1.27	0.27
Al_2O_3	15.19	16.52	15.38	16.75	16.85	17.22	16.66	17.43	18.67	17.42
Fe_2O_3	5.70	4.02	4.06	4.23	5.60	6.16	3.59	4.26	4.57	4.80
FeO	3.83	5.22	5.50	1.74	1.83	0.89	2.48	1.20	3.15	0.20
MgO	8.66	7.19	10.48	0.56	1.02	0.96	0.65	0.66	2.14	0.03
MnO	0.158	0.133	0.169	0.174	0.195	0.222	0.182	0.186	0.135	0.141
CaO	9.95	7.91	10.56	2.28	3.28	3.74	2.59	2.30	5.75	0.20
Na_2O	2.79	4.16	3.05	5.96	5.62	5.88	6.08	5.90	5.42	6.55
K_2O	1.38	2.17	1.36	3.96	3.52	3.67	4.13	3.81	3.20	4.78
P_2O_5	0.347	0.693	0.295	0.137	0.253	0.282	0.147	0.162	0.614	0.034
F	0.096	0.101	0.106	0.046	0.104	n.d.	0.032	n.d.	0.071	n.d.
CO_2	0.21	0.05	0.11	0.02	< 0.01	0.06	0.01	0.02	0.01	0.01
S(tot.)	< 0.010	< 0.010	< 0.010	< 0.010	0.011	< 0.010	< 0.010	0.011	< 0.010	0.037
H_2O^+	1.13	1.51	0.53	0.43	1.52	0.59	0.21	0.78	0.60	1.07
H_2O^-	0.35	0.21	0.22	0.08	0.14	0.08	< 0.05	0.18	0.09	0.13
Total	99.44	99.54	99.52	99.12	99.16	99.49	99.57	99.28	99.70	99.06
Cr	362.2	124.8	343.5	3.5	3.1	0.5	2.2	0.9	9.5	1.0
Ga	16.8	18.1	14.6	19.6	20.6	21.8	21.2	22.6	21.6	37.6
Hf	2.5	2.9	3.3	4.0	3.9	6.5	4.5	7.5	3.9	22.2
Nb	55.2	58.6	35.0	68.5	83.9	208.0	81.3	217.9	98.7	415.8
Ni	126.4	99.8	123.9	11.6	10.8	18.7	8.2	18.0	14.9	16.9
Pb	39.0	10.7	0.9	13.6	10.10	7.1	13.8	21.3	23.4	27.4
Rb	24.5	39.6	34.3	53.2	73.0	96.9	74.3	125.2	91.0	131.6
Ta	10.9	9.3	< 5.0	9.4	22.5	26.7	11.1	28.0	34.8	48.1
Th	7.1	6.4	8.7	14.0	13.4	14.0	15.1	16.8	16.1	22.1
U	1.4	2.0	0.7	4.8	3.6	2.8	4.2	3.3	4.4	4.7
V	234.6	183.1	206.4	7.8	8.1	12.2	5.2	13.0	92.4	5.6
Zr	126.6	183.1	118.1	284.5	264.0	273.3	300.8	317.5	269.7	1020.0
Sr	558.5	939.5	774.0	311.5	446.6	495.9	331.6	360.3	792.5	15.5
Sc	33.9	26.9	< 1.0	15.9	14.5	< 1.0	16.8	3.6	16.2	4.2
Ba	560.0	753.0	507.5	1333.0	1258.5	1143.2	1391.0	1224.4	1132.5	37.8
Y	16.96	16.90	19.26	28.26	28.55	29.84	31.22	28.62	24.02	79.49
La	36.2	40.3	41.4	87.0	88.1	77.7	94.1	72.9	99.8	139.2
Ce	58.0	65.7	75.1	133.7	136.7	131.9	145.5	122.4	146.7	248.1
Pr	6.27	7.10	7.56	13.60	14.00	13.44	14.24	12.34	14.03	26.28
Nd	23.9	27.9	27.8	45.5	49.0	40.6	49.6	35.4	48.0	81.6
Sm	4.26	4.92	4.68	7.05	7.56	6.11	7.50	5.66	6.90	13.99
Eu	1.580	1.775	1.425	2.240	2.650	2.125	2.365	1.695	2.470	1.190
Gd	3.57	4.02	4.55	6.92	6.93	6.45	6.76	5.57	6.52	13.36
Tb	0.567	0.626	0.635	0.959	0.999	0.900	1.008	0.755	0.850	2.015
Dy	3.52	3.65	3.66	5.72	5.92	4.72	6.32	4.19	4.96	11.54
Ho	0.675	0.700	0.730	1.140	1.160	1.025	1.230	0.815	0.975	2.230
Er	1.79	1.72	2.13	3.24	3.27	2.94	3.57	2.59	2.64	6.80
Tm	0.247	0.228	0.280	0.503	0.489	0.440	0.522	0.360	0.394	0.955
Yb	1.72	1.51	2.01	3.51	3.41	2.91	3.83	2.48	2.61	6.36
Lu	0.265	0.250	0.295	0.595	0.560	0.465	0.640	0.380	0.435	0.985

n.d. – not determined

rated by noticeable gap in the LREE contents. Whereas trachyandesites and trachytes share practically identical LREE contents, the basaltic rocks are significantly poorer in these elements. In addition, partly in trachyandesites but mainly in trachytes, the depletion of MREE compared to HREE and progressively developing U-shaped

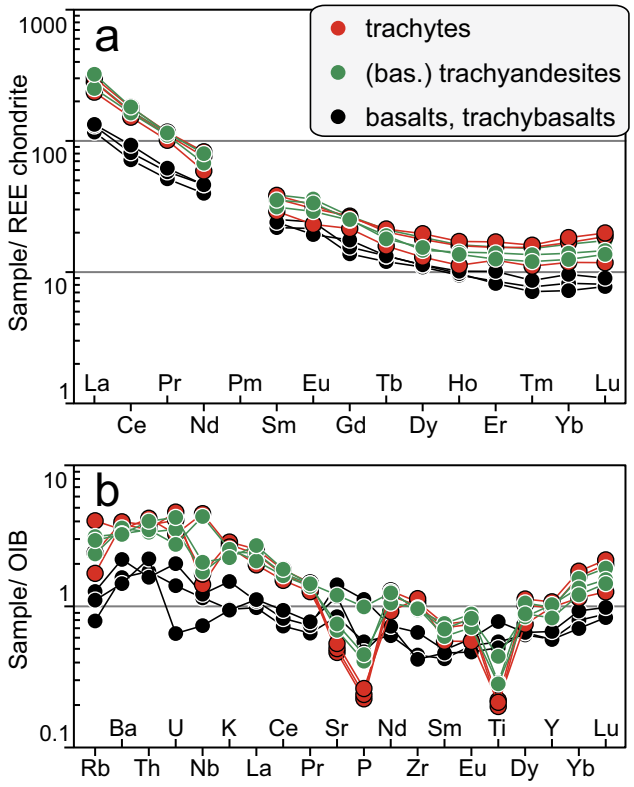

Fig. 7 Spider plots for trace-element compositions obtained in the current work and normalized to average chondrite (Boynton 1984) (**a**) and ocean-island basalt, OIB (Sun and McDonough 1989) (**b**).

(convex down) REE patterns can be noticed. Absence of Eu anomaly suggests that the plagioclase fractionation did not play any significant role in differentiation of the studied suite.

The basaltic samples resemble the typical ocean-island basalt (OIB) compositions, as demonstrated by OIB-normalized spiderplot (Sun and McDonough 1989; Fig. 7b). Moreover, the LREE enrichment in more differentiated (more siliceous) rock types is accompanied by enrichment in other incompatible elements, such as Rb, Ba, Th, U as well as, in some samples, development of a Nb trough.

4.6. Geochronology

New geochronological data have been used to support the reconstruction of the North Chamo Volcanic Field evolution. Five representative volcanic samples were selected for K/Ar dating. The analytical data are presented in Tab. 2, and the sampling sites are shown on Fig 1.

The K/Ar ages obtained on these samples range between 1.86 ± 0.13 Ma (Alakom Hill, trachybasalt, VR021) and 0.44 ± 0.15 Ma (Ganta trachyte, VR026D), respectively.

The highest obtained age from trachybasalt of Alakom Hill (1.86 ± 0.13 Ma) corresponds well with the erosional level of this cone exposing its feeding conduit. The better preserved Kale Korke scoria cone located in the Nech Sar plains provided rather older age of 1.05 ± 0.46 Ma. Despite the large analytical error – caused by the high atmospheric argon contamination – the apparent age can be correlated with published ages of basaltic lavas from Tosa Sucha and adjacent part of Nech Sar (K–Ar: 1.34–0.68 Ma: Ebinger et al. 1993; George and Rogers 1999).

On the other hand, the pyroclastic cones within northern Chamo Lake and on its banks are characterized by rather uniform ages of *c.* 0.5 Ma (Tab. 2) with striking consistency. Despite that the trachyandesite VR028 provided slightly higher age (0.52 ± 0.08 Ma) than the Ganta trachyte (VR026D = 0.44 ± 0.15 Ma), the geological evidence shows trachyandesite lava overlaying the Ganta pyroclastic deposits (Fig. 3). Nevertheless, this discrepancy remains within analytical error, suggesting that both eruptions occurred shortly after each other. Although it may be argued that these determinations do not represent the real eruption ages precisely, they do indicate that an important, and until now final, eruption event in this area occurred in Middle Pleistocene.

4.7. Radiogenic isotopes

4.7.1. Sr–Nd isotopes

Seven newly acquired Sr–Nd isotopic pairs from the North Chamo Volcanic Field, and one from the country-rock ignimbrite, are given in Tab. 3. In figures, these data are supplemented by 10 Sr and 11 Nd isotopic analyses of Tosa Sucha volcanic rocks obtained by George and Rogers (1999).

In general, the measured Sr isotopic ratios in our new data set do not vary much ($^{87}Sr/^{86}Sr$ = 0.7033–0.7038; Tab. 3) and compare well with the literature data (Fig. 8a). Only the ignimbrite TH615 contains much elevated present-day $^{87}Sr/^{86}Sr$ of 0.7162. However, Nd is more variable; six samples (without the trachyte VR026D) give $^{143}Nd/^{144}Nd$ of 0.51275–0.51283, translating to ε_{Nd} of +2.2 to +3.8 (Tab. 3). The ignimbrite TH615 falls at

Tab. 2 K–Ar data obtained on Pleistocene volcanic rocks from the North Chamo and Nech Sar areas

Sample (lab. No.)	Rock	K (%)	$^{40}Ar_{rad}$ (ccSTP/g)	$^{40}Ar_{rad}$ (%)	Age (Ma ± 1σ)
VR020 (8326)	Bomb (olivine basalt)	1.176	4.8424×10^{-8}	3.3	1.05 ± 0.46
VR021	Trachybasalt	1.853	1.3457×10^{-8}	19.9	1.86 ± 0.13
VR025	Olivine basalt	1.069	2.3197×10^{-8}	2.9	0.55 ± 0.27
VR026D	Trachyte	2.904	4.9307×10^{-8}	4.0	0.44 ± 0.15
VR028	Trachyandesite	2.134	4.287×10^{-8}	8.8	0.52 ± 0.08

Tab. 3 Sr–Nd isotopic data

Sample	Rock	MgO (wt. %)	Rb (ppm)	Sr (ppm)	$^{87}Sr/^{86}Sr$	2 s.e.	Sm (ppm)	Nd (ppm)	$^{143}Nd/^{144}Nd$	2 s.e.	ε_{Nd}
VR025	olivine basalt	10.48	34.3	774.0	0.70344	0.000008	4.68	27.8	0.512809	0.000016	3.34
VR020	olivine basalt (bomb)	8.66	24.5	558.5	0.70347	0.000018	4.26	23.9	0.512832	0.000009	3.78
VR021	trachybasalt	7.19	39.6	939.5	0.70330	0.000009	4.92	27.9	0.512801	0.000006	3.18
VR028	trachyandesite	2.14	91.0	792.5	0.70345	0.000009	6.90	48.0	0.512755	0.000009	2.28
VR026C2	trachyandesite (bomb)	0.96	96.9	495.9	0.70384	0.000020	6.11	40.6	0.512770	0.000010	2.57
VR026D2	trachyte	0.66	125.2	360.3	0.70373	0.000017	5.66	35.4	0.512751	0.000009	2.20
VR026D	trachyte	0.65	74.3	331.6	0.70367	0.000012	7.50	49.6	0.512703	0.000005	1.27
TH615	ignimbrite	0.03	131.6	15.5	0.71622	0.000007	13.99	81.6	0.512745	0.000007	2.09

s.e. – standard error of the mean

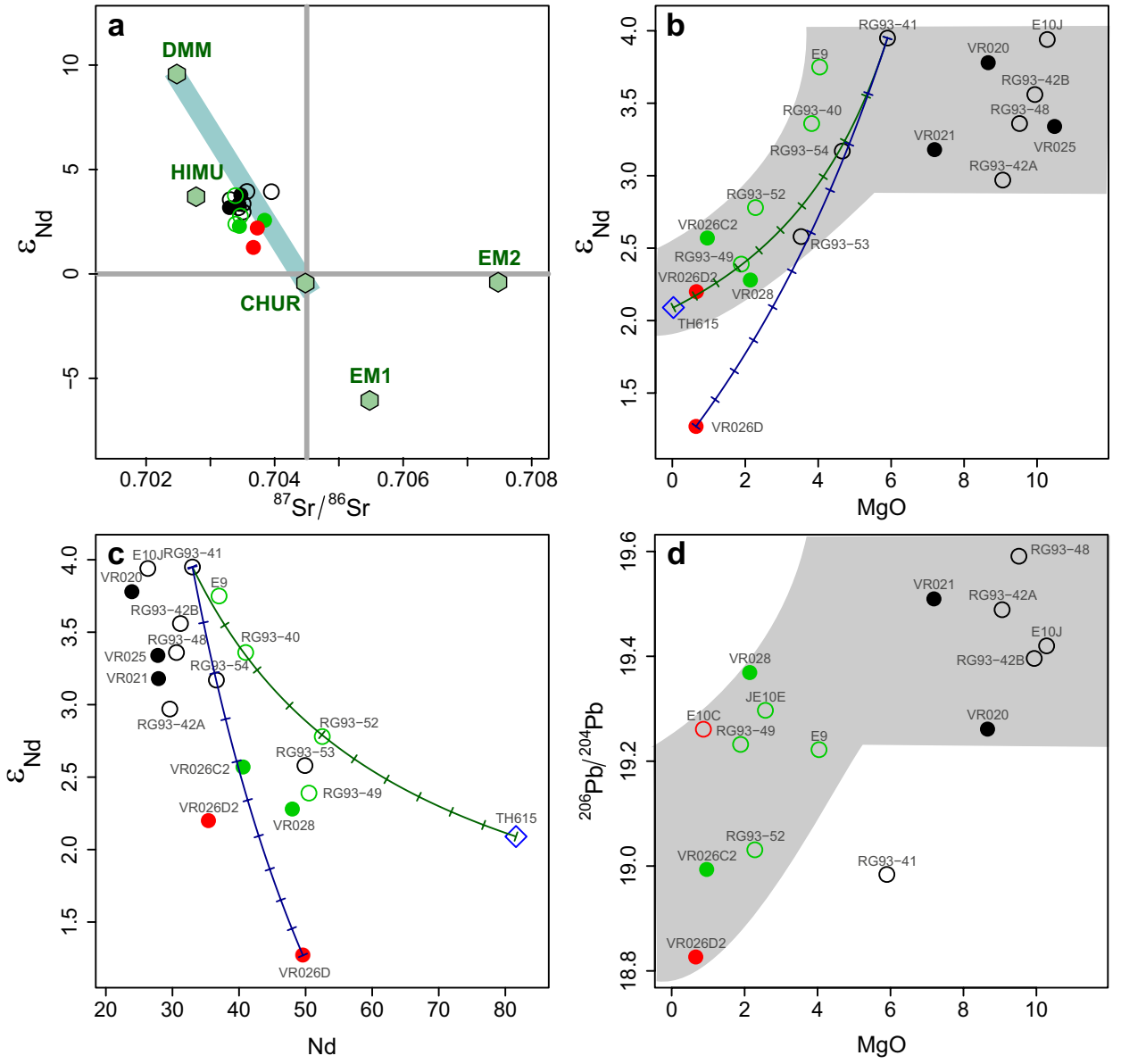

Fig. 8 The Sr–Nd–Pb isotopic data. **a** – Whole-rock $^{87}Sr/^{86}Sr$ vs. ε_{Nd} plot for the newly-obtained dataset complemented with data from George and Rogers (1999). For reference are shown compositions of the Chondritic Uniform Reservoir (CHUR) (Nd: Jacobsen and Wasserburg 1980; Sr: Faure 1986), Depleted MORB Mantle (DMM) (Nd: Liew and Hofmann 1988; Sr: Rehkämper and Hofmann 1997), Enriched Mantle 1 and 2 (EM1 and EM2: Hart 1988) and High-μ Mantle (HIMU: Hart 1988). **b** – Binary plot MgO vs. ε_{Nd}. **c** – Binary plot Nd vs. ε_{Nd}. **d** – Binary plot MgO vs. $^{206}Pb/^{204}Pb$. The hyperbolae in (b–c) with 10% tick marks are the result of direct modelling of binary mixing between basalt RG93-41 of George and Rogers (1999) and, respectively, country-rock ignimbrite TH615 or the trachyte VR026D (Tabs 1, 3).

Tab. 4 Lead isotopic data

Sample	Rock	MgO (wt. %)	U	Th	Pb	$^{206}Pb/^{204}Pb$	2 s.e.	$^{207}Pb/^{204}Pb$	2 s.e.	$^{208}Pb/^{204}Pb$	2 s.e.	$^{207}Pb/^{206}Pb$	2 s.e.	$^{208}Pb/^{206}Pb$	2 s.e.
VR020	olivine basalt	8.66	1.4	7.1	39.0	19.2612	0.0022	15.6445	0.0018	39.3172	0.0044	0.81201	0.00002	2.04148	0.00004
VR021	trachybasalt	7.19	2.0	6.4	10.7	19.5096	0.0021	15.6223	0.0017	39.3131	0.0043	0.80060	0.00002	2.01538	0.00003
VR028	trachyandesite	2.14	4.4	16.1	23.4	19.3691	0.0019	15.6353	0.0016	39.3831	0.0040	0.80703	0.00002	2.03364	0.00003
VR026C2	trachyandesite	0.96	2.8	14.0	7.1	18.9936	0.0017	15.6260	0.0013	39.0688	0.0035	0.82245	0.00001	2.05731	0.00003
VR026D2	trachyte	0.66	3.3	16.8	21.3	18.8266	0.0015	15.6142	0.0012	38.9189	0.0031	0.82906	0.00001	2.06744	0.00003

the less radiogenic end of this interval ($^{143}Nd/^{144}Nd$ = 0.51275, ε_{Nd} = +2.1). Finally, trachyte VR026D contains the least radiogenic Nd ($^{143}Nd/^{144}Nd$ = 0.51270, ε_{Nd} = +1.3). Overall, the Nd isotopic composition shows a remarkable evolution with increasing degree of differentiation (decreasing MgO: Fig. 8b). After the first, roughly subhorizontal segment, when ε_{Nd} values scatter roughly between +4 and +3, they drop rapidly to ca. +2 as MgO ~ 0 is approached. This illustrates an open-system behaviour of the magmas parental to the less magnesian (MgO smaller than ca. 6 wt. %) members of the studied volcanic suite.

4.7.2. Pb isotopes

Five newly acquired Pb isotopic compositions from the North Chamo Volcanic Field are given in Tab. 4. In figures, these data are supplemented by 10 Pb isotopic analyses of Tosa Sucha volcanic rocks by George and Rogers (1999). In general, the measured Pb isotopic ratios of our data set compare well with the literature data (Fig. 9). Due to very low age, the Pb isotopic data have not been age corrected. The North Chamo Volcanic Field samples have elevated $^{207}Pb/^{204}Pb$ (15.614–15.646) and $^{208}Pb/^{204}Pb$ (38.919–39.383) at a given $^{206}Pb/^{204}Pb$ (18.827–19.510) compared to the Northern Hemisphere Reference Line (NHRL: Hart 1984) (Fig. 9). The Pb isotopic composition of the North Chamo Volcanic Field plots into range already observed for the Northern transect basalts of southern Ethiopia (NTS) and partly to its overlap with the Afar and Gulf of Aden group. Our data

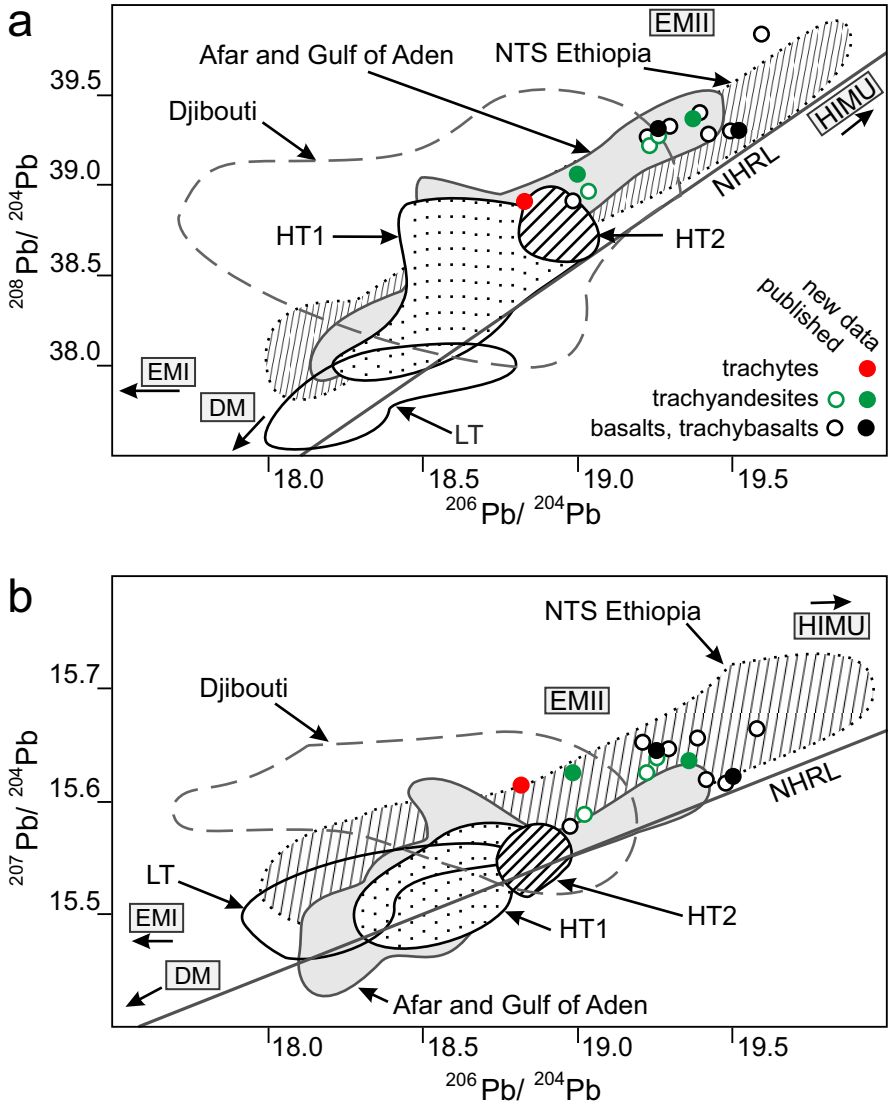

Fig. 9 Lead isotopic composition diagrams for the North Chamo Volcanic Field rocks, modified after Meshesha and Shinjo (2007): **a** – $^{206}Pb/^{204}Pb$ vs. $^{208}Pb/^{204}Pb$; and **b** – $^{206}Pb/^{204}Pb$ vs. $^{207}Pb/^{204}Pb$. For comparison are shown other data from the adjacent parts of the East African Rift System, Djibouti basalts (Deniel et al. 1994), Afar and Gulf of Aden basalts (Schilling et al. 1992), Low-Ti (LT), Intermediate-Ti (HT1) and High-Ti (HT2) basalts (Pik et al. 1999) and Northern transects basalts (NTS) of southern Ethiopia (Stewart and Rogers 1996). Compositions of Depleted Mantle (DM), HIMU and Enriched Mantle (EMI and EMII) reservoirs are taken from Zindler and Hart (1986).

define a trend subparallel to NHRL in conventional Pb isotope diagrams. In detail, most radiogenic samples of our set are trachybasalt VR021 and trachyandesite VR028, representing the oldest and the youngest rocks studied. Trachyandesite VR026C2 and larger pyroclasts of olivine basalt VR020 have intermediate Pb isotopic composition; the least radiogenic is trachyte VR026D2. For Pb isotopic compositions can be seen the same open-system behaviour as for Nd isotopes. The Pb isotopes evolve to less radiogenic values with increasing degree of differentiation (Fig. 8d) whereby $^{206}Pb/^{204}Pb$ values drop rapidly with decreasing MgO content (for MgO < 6 wt. %).

5. Discussion

5.1. Evolution of eruptive styles

Unlike the simple eruptive scenario of Strombolian scoria cones on Nech Sar plains, the pyroclastic cones and rings in the northern Chamo Lake and on its banks have experienced events of variable explosivity. Basal layer of the Ganjulle scoria cone consists of poorly sorted deposits dominated by angular juvenile fragments of non-vesicular olivine basalt (Fig. 2e) suggesting phreatomagmatic eruption of Surtseyan style. The phreatomagmatic deposits are overlain by basaltic scoriae of the same composition.

Such a transition of eruption style from phreatomagmatic towards Strombolian is rather common at monogenetic pyroclastic cones. It usually reflects growth of the pyroclastic cone above the water level (i.e. in marsh or shallow lake) when the erupted magma is no more affected by quench-fragmentation (e.g., Schmincke 1977; Clarke et al. 2009; Kereszturi et al. 2014; Kshirsagar et al. 2016). The initial Surtseyan (phreatomagmatic) phase of the Ganjulle Volcano created an island in the Chamo Lake. Following magmatic activity was then insulated from the water body and built up a scoria cone. Thin horizon of weathering products indicates a short break in eruptive activity. Renewed eruption then continued in Strombolian style.

Ganta cone on the other hand reveals a more complex evolution. The deposits of phreatomagmatic (Surtseyan) phase here are underlain by trachytic pumice with highly vesiculated trachyte lava at the base. The trachyte lava displays no sign of magma–water interaction (e.g., inhibition of vesiculation, angular fragmentation). The pumice then shows a systematic decrease in grain size towards the level of transition into the trachyandesitic phreatomagmatic deposit. The chemical transition can be explained in terms of exhaustion of a compositionally zoned magma chamber as described from numerous ignimbrite-forming eruptions (e.g., Milner et al. 2003; Hildreth and Wilson 2007; Bachmann and Bergantz 2008).

In the case of monogenetic volcanoes, the existence of compositionally heterogeneous chamber(s) or multiple magma injections are mostly reflected in magma mingling textures (e.g., Németh et al. 2003; Rapprich et al. 2017), whereas compositionally zoned pyroclastic deposits are infrequent. The Ganta cone apparently gives an evidence that also small monogenetic volcanoes may be associated with a zoned chamber, producing a compositionally zoned pyroclastic deposit during exhausting eruption. The shift in eruption style from Strombolian or Sub-Plinian to phreatomagmatic (Surtseyan) might reflect rise of water level in the Chamo Lake. Given the large areal extent of this lake, increase in water level within a short event (during a single eruption) is rather unlikely. On the other hand, there are many pieces of evidence for significant tectonic displacements synchronous with, and post-dating the volcanic activity in the study area (see Section 4.2 and Fig. 1). The banks of Chamo Lake were probably subject to tectonic subsidence during initial phase of Ganta cone activity, resulting in shift towards Surtseyan eruption style. Ongoing eruption building up a cone led to the extrication of the eruption from the lake-water influence.

The characteristic appearance of Ganta pyroclastic deposits with obvious compositional zoning allowed correlating of Ganta cone with pyroclastic deposit beneath the trachyandesite lava in the road-cut in serpentines on the southern edge of Arba Minch. Analytical age of the Ganta cone (0.44 ± 0.15 Ma) is lower than that of the trachyandesite lava exposed in several tectonically offset blocks in and south of Arba Minch (0.52 ± 0.08 Ma), but the difference is within the analytical error. Both volcanic rocks probably erupted within a relatively short interval during Middle Pleistocene (at *c.* 0.5 Ma). No other volcanic product covering the Arba Minch trachyandesite lava was documented.

5.2. On the importance of crustal assimilation and its combination with fractional crystallization

The MgO vs. ε_{Nd}, Nd vs. ε_{Nd} and MgO vs. $^{206}Pb/^{204}Pb$ plots (Fig. 8b–d) illustrate well open-system behaviour of more evolved lithologies sampled in course of the present study. At the first approximation, the variation can be reproduced by simple direct binary mixing model (Janoušek et al. 2016) between basalt RG93-41 of George and Rogers (1999) and country-rock ignimbrites of the earlier (Oligocene–Pleistocene) volcanic phase, represented by the sample TH615. The mixing curve fits rather well the observed variation of samples with MgO < 6 wt. %, suggesting that the initial (essentially) closed-system crystallization was replaced by assimilation of the potentially fertile ignimbrites, most likely coupled with fractional crystallization (AFC: DePaolo 1981). In fact,

the assimilant could have had less Nd with slightly less radiogenic composition than the sample TH615, as demonstrated by the second modelled mixing curve, passing through the trachyte VR026D.

In any case, the assimilation model seems to be supported also by incompatible trace-element data, as their contents do not increase continuously with differentiation (decreasing MgO). Significant gap between basalts and trachyandesites in concentrations of LILE and LREE is not mimicked by a similar shift when comparing trachyandesites and trachytes. On the other hand, the negative Sr–P and Ti anomalies, most likely controlled by fractionation of apatite and titanite, deepen progressively during differentiation. The depletion of MREE compared to HREE and gradually developing U-shaped (convex down) REE patterns of trachytic rocks then point to fractionation of amphibole and/or titanite (e.g., Davidson et al. 2013 and Žák et al. 2009 with references therein).

5.3. Thermodynamic modelling

In order to test and further constrain the potential role of the open-system processes, we have undertaken thermodynamic modelling by the Magma Chamber Simulator (MCS) (Bohrson et al. 2014, 2020). Our intention was to model the entire available dataset, including the literature data of George and Rogers (1999) and Rooney (2010). Moreover, we wanted to avoid the uncertainty in the choice of distribution coefficients for individual rock-forming minerals and the necessity to assess the role of accessories (Janoušek et al. 2016). Therefore, solely major elements, without trace elements or radiogenic isotopes, have been taken into account, using the *PhaseEQ* module of the MCS.

Given the variation of the radiogenic isotopes, the preferred scenario was a simple fractional crystallization, joined only later by assimilation of wall-rock-derived partial melts (MCS-AFC). In this model, sensible heat (melt cooling) and latent

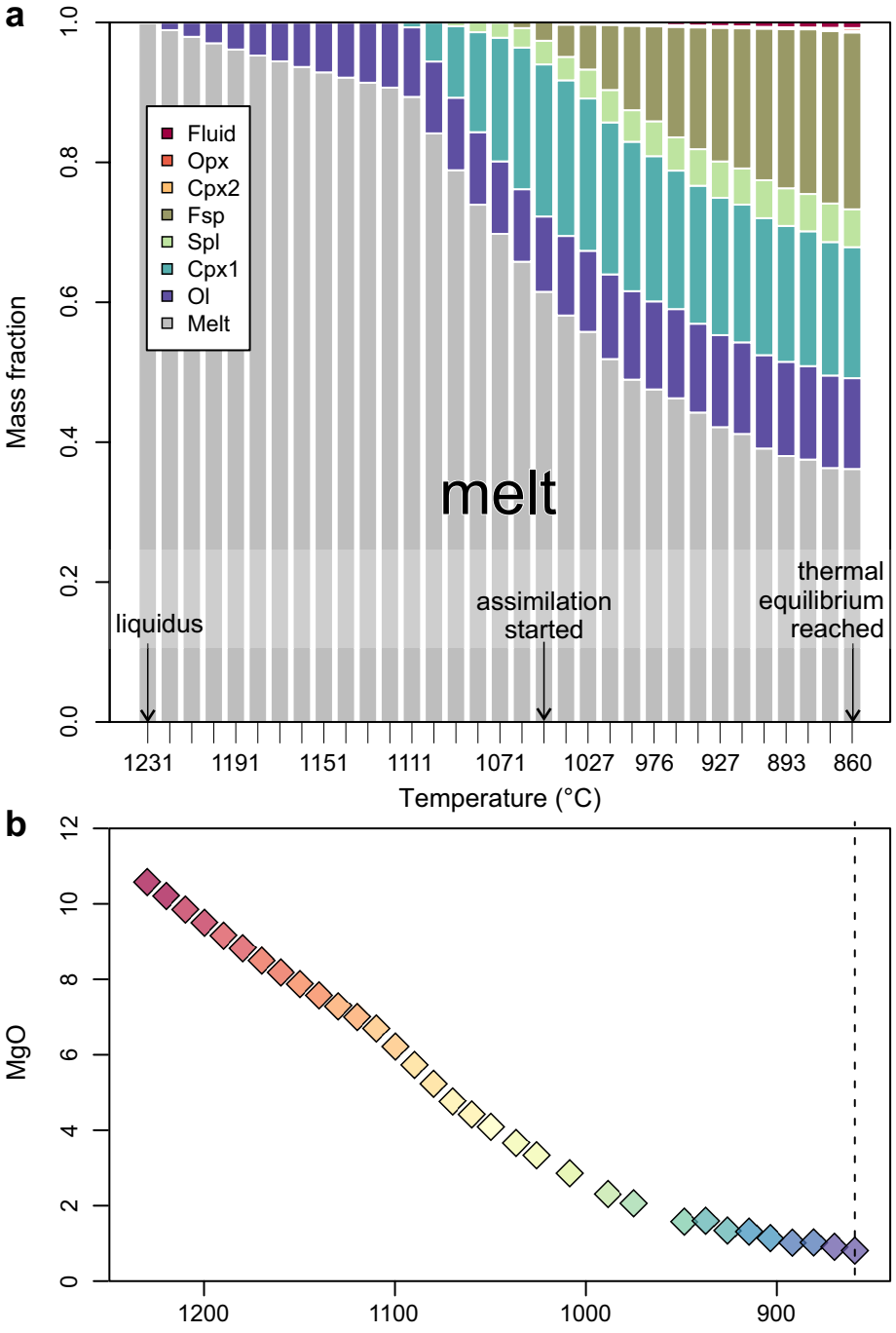

Fig. 10 Results of the MCS-AFC simulation [shallow, isobaric (1 kbar) crystallization of a melt corresponding to VR025 being progressively contaminated by the partial melts of country-rock ignimbrite TH615]. **a** – Mass fractions of the individual phases (melt, fluid, crystallizing minerals) as a function of temperature (°C). Please note that the temperatures for the steps including assimilation are not spaced equidistantly. **b** – MgO contents (wt. %) in the modelled cooling melt. For explanation and details of the model, see text, as well as ESM 6 and 7.

heat (crystallization) generated in the magma subsystem are transferred through the magma chamber–wall-rock interface and heat the country rock. If the heating is sufficient, the wall-rock melting commences. As soon as the amount of the thus generated melt exceeds the prescribed percolation threshold, any surplus melt is transferred to the main magma reservoir, mixed and equilibrated thoroughly (Heinonen et al. 2022).

In our run, the liquidus of the modelled magma composition (corresponding, except the volatiles, to the sample VR025) was determined at 1231 °C (Fig. 10). The melt percolation threshold ("FmZero") of 5 % was reached when the wall-rock was at c. 695 °C and the main magma reservoir at 1050 °C. From this point on, the magma experienced a more rapid cooling, shown by significantly broader spacing of the individual modelling steps. The simulation stopped at ca. 860 °C, when the thermal equilibrium was attained between the two subsystems, i.e. magma and wall-rock.

The total modelled amount of assimilated wall-rock material was considerable, 24 wt. %. The crystallization succession, as portrayed in Fig. 10, included the following phases (in brackets is the approximate temperature of the modelling step when the given mineral appeared): olivine (liquidus of 1231 °C; $Fo_{0.88} \rightarrow Fo_{0.50}$) → clinopyroxene 1 (1110 °C; diopside) → spinel (1090 °C) → feldspar (1070 °C; changing from bytownite to anorthoclase, $K_{0.00}Na_{0.15}Ca_{0.85} \rightarrow K_{0.05}Na_{0.65}Ca_{0.30}$) → clinopyroxene 2 (1040 °C) → orthopyroxene (870 °C); hydrous fluid appeared at *c.* 1010 °C.

Overall, the modelled trends reproduce reasonably well the chemical evolution of the North Chamo Volcanic Field and Tosa Sucha Volcano. Examples shown here include the TAS diagram (Fig. 11), as well as the Fenner plots (Fig. 12). Thus we conclude that the magmas parental to the North Chamo alkaline volcanics likely evolved in two steps. The initial stage was a closed-system fractionation of an Ol–Cpx–Spl–Pl assemblage, producing alkali basalts, trachybasalts, and basaltic trachyandesites. The subsequent stage – yielding trachyandesites and trachytes – was characterized by a substantial contamination (AFC-style processes) by earlier (Paleogene) acidic volcanic products, exemplified by the ignimbrite sample TH615. This underlines the complexity of sources tapped and processes shaping volcanism in the southern extremity of the Main Ethiopian Rift.

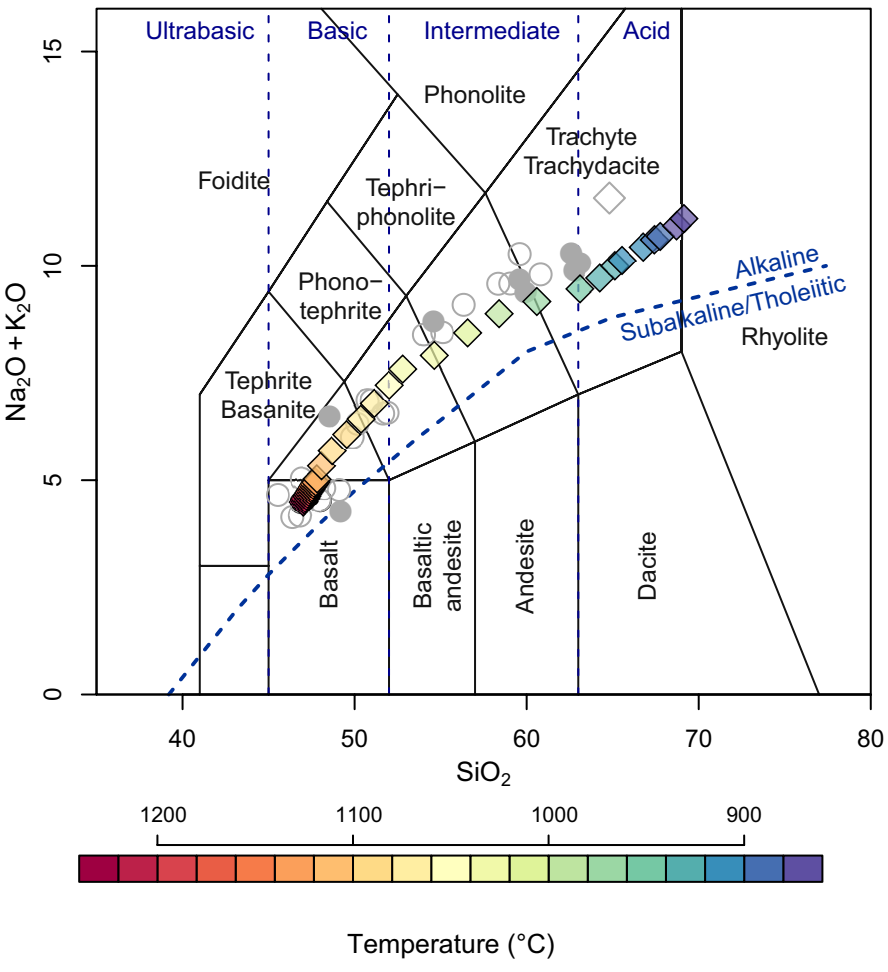

Fig. 11 The Total Alkalis–Silica (TAS) diagram (Le Maitre et al. 2002) with results of the MCS-AFC simulation colour-coded by temperature. Real analyses from the North Chamo Volcanic Field are grey.

6. Conclusions

- The volcanic activity of the North Chamo Volcanic Field at southern termination of the Main Ethiopian Rift was partly synchronous, and partly post-dated eruptions of the Tosa Sucha Volcano (*c.* 1.3–0.7 Ma), but no evidence for activity younger than the Middle Pleistocene (*c.* 0.45 Ma) was found.
- The observed transition towards phreatomagmatic eruption style suggests that the tectonic extension associated with subsidence was contemporaneous with the volcanic activity. On the other hand, the change from phreatomagmatic (Surtseyan) towards Strom-

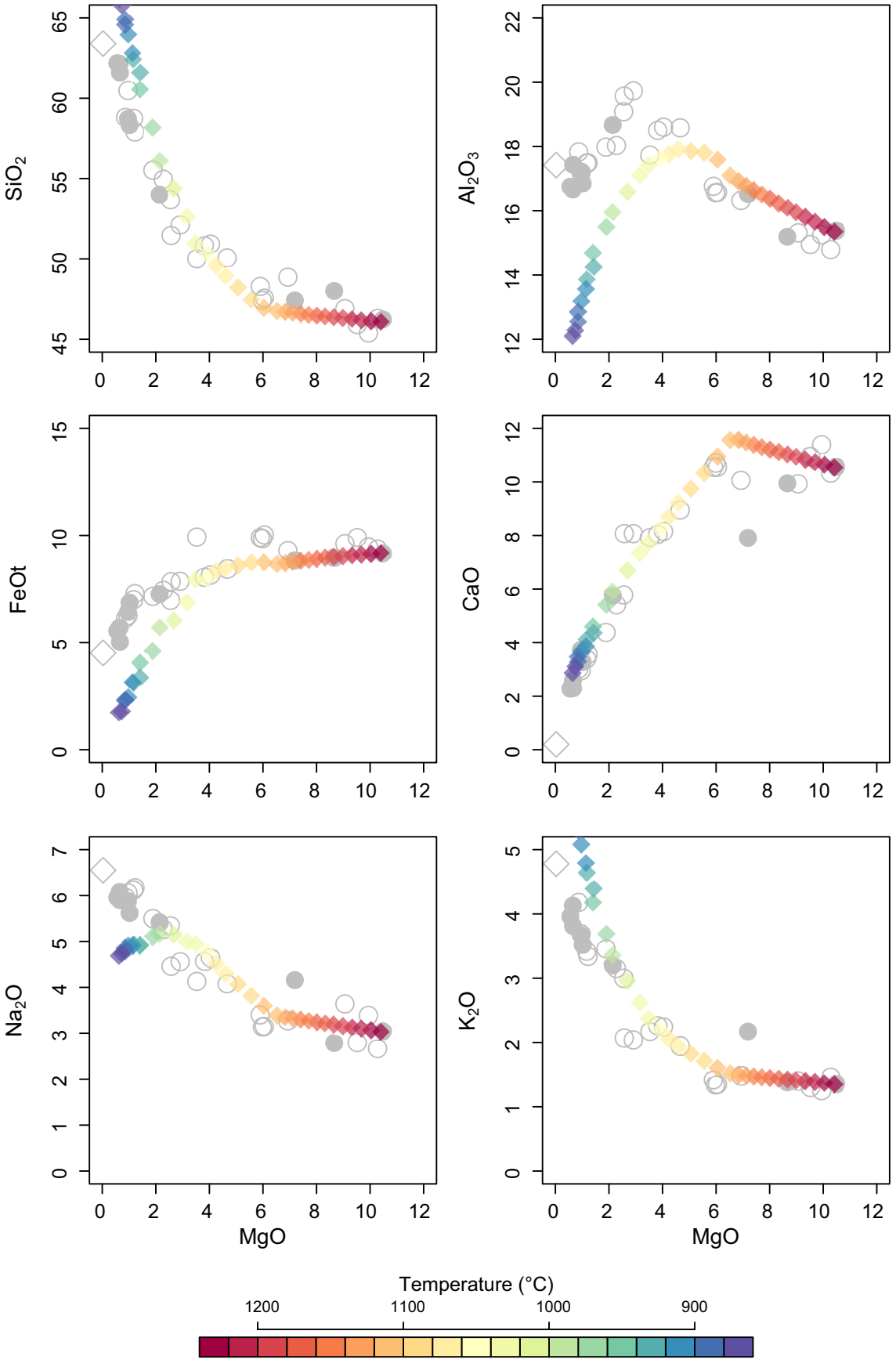
SiO2
Al2O3
FeOt
CaO
Na2O
K2O
MgO
MgO
Temperature (°C)
1200
1100
1000
900

bolian eruption style can be explained in terms of pyroclastic cone growth up from the wet-land/shallow lake.

- The studied rocks show a broad compositional range from alkali basalt, through trachybasalt and trachyandesite to trachyte. The Sr–Nd–Pb isotopic variation, supported by major-elements-based thermodynamic modelling, demonstrate that magmas parental to the North Chamo alkaline volcanic rocks (alkali basalt, through trachybasalt and trachyandesite to trachyte) evolved initially by closed-system fractionation of olivine, clinopyroxene, spinel and calcic plagioclase. The subsequent stage was characterized by a substantial assimilation of country-rock felsic igneous material, represented by Paleogene ignimbrites.

Acknowledgements. The research of the North Chamo Volcanic Field was carried out within the framework of Czech–Ethiopian development cooperation focused on natural hazards, financially supported by the Czech Development Agency. Programming and deployment of software tools for numerical modelling of magma evolution were supported by the Czech Science Foundation (GACR, project 22-34175S to VJ). This manuscript contributes to the Strategic Research Plan of the Czech Geological Survey (DKRVO/ČGS 2018–2022), project 310950. Quality of the manuscript benefited from comments by reviewers Prokop Závada and Dereje Ayalew, as well as by handling editor Václav Kachlík.

Electronic Supplementary Material. Selected electron-microprobe analyses of the main and accessory rock-forming minerals, settings (MES) file and complete spreadsheet with the Magma Chamber Simulator (MCS) modelling output are available at the Journal web site (*http://dx.doi.org/10.3190/jgeosci.365*).

References

Ayalew D, Getaneh W, Pik R, Atnafu B, Zemelak A, Belay E (2021) Stratigraphic framework of the northeastern part of the Ethiopian flood basalt province. Bull Volcanol 83: 1–13

Bachmann O, Bergantz GW (2008) Deciphering magma chamber dynamics from styles of compositional zoning in large silicic ash flow sheets. In: Putirka KD, Tepley III FJ (eds) Minerals, Inclusions and Volcanic Processes. Reviews in Mineralogy and Geochemistry 69, pp 651–674

⇦

Fig. 12 Fenner diagrams with results of the MCS-AFC simulation colour-coded by temperature. Real analyses from the North Chamo Volcanic Field are grey.

Balogh K (1985) K/Ar Dating of Neogene Volcanic Activity in Hungary: Experimental Technique, Experiences and Methods of Chronologic Studies. ATOMKI Rep., D/1: pp 277–288

Barrat JA, Joron JL, Taylor RN, Fourcade S, Nesbitt RW, Jahn BM (2003) Geochemistry of basalts from Manda Hararo, Ethiopia: LREE-depleted basalts in Central Afar. Lithos 69: 1–13

Berhanu G (2019) Geology, petrology and geochemistry of volcanic rocks around Arba Minch, southern Ethiopia. Earth Sci 8: 160–168

Biggs J, Ayele A, Fischer TP, Fontijn K, Hutchison W, Kazimoto E, Whaler K, Wright TJ (2021) Volcanic activity and hazard in the East African Rift Zone. Nature Commun 12: 6881. DOI: 10.1038/s41467-021-27166-y

Bohrson WA, Spera FJ, Ghiorso MS, Brown GA, Creamer JB, Mayfield A (2014) Thermodynamic model for energy-constrained open-system evolution of crustal magma bodies undergoing simultaneous recharge, assimilation and crystallization: the Magma Chamber Simulator. J Petrol 55: 1685–1717

Bohrson WA, Spera FJ, Heinonen JS, Brown GA, Scruggs MA, Adams JV, Takach MK, Zeff G, Suikkanen E (2020) Diagnosing open-system magmatic processes using the Magma Chamber Simulator (MCS): part I – major elements and phase equilibria. Contrib Mineral Petrol 175: 104

Bouvier A, Blichert-Toft J, Vervoort JD, Albarède F (2005) The age of SNC meteorites and the antiquity of the Martian surface. Earth Planet Sci Lett 240: 221–233

Boynton WV (1984) Cosmochemistry of the rare earth elements: meteorite studies. In: Henderson P (ed) Rare Earth Element Geochemistry. Developments in Geochemistry. Elsevier, Amsterdam–New York, pp 63–114

Clarke H, Troll VR, Carracedo JC (2009) Phreatomagmatic to Strombolian eruptive activity of basaltic cinder cones: Montana Los Erales, Tenerife, Canary Islands. J Volcanol Geotherm Res 180: 225–245

Corti G (2009) Continental rift evolution: from rift initiation to incipient break-up in the Main Ethiopian Rift, East Africa. Earth Sci Rev 96: 1–53

Davidson J, Turner S, Plank T (2013) Dy/Dy*: variations arising from mantle sources and petrogenetic processes. J Petrol 54: 525–537

Dempírová L, Šikl J, Kašičková R, Zoulková V, Kříbek B (2010) The evaluation of precision and relative error of the main components of silicate analyses in Central Laboratory of the Czech Geological Survey. Zpr Geol Výzk v Roce 2009: 326–330 (in Czech with English summary)

Deniel C, Vidal P, Coulon C, Vellutini PJ, Piguet P (1994) Temporal evolution of mantle sources through continental rifting: the volcanism of Djibouti (Afar). J Geophys Res 99: 2853–2869

DePaolo DJ (1981) Trace element and isotopic effects of combined wallrock assimilation and fractional crystallization. Earth Planet Sci Lett 53: 189–202

Ebinger CJ, Yemane T, WoldeGabriel G, Aronson JL, Walter RC (1993) Late Eocene–Recent volcanism and faulting in the southern main Ethiopian rift. J Geol Soc, London 150: 99–108

Faure G (1986) Principles of Isotope Geology, 2nd edition. John Wiley & Sons, Chichester, pp 1–589

Fontijn K, McNamara K, Tadesse AZ, Pyle DM, Dessalegn F, Hutchison W, Mather TA, Yirgu G (2018) Contrasting styles of post-caldera volcanism along the Main Ethiopian Rift: implications for contemporary volcanic hazards. J Volcanol Geotherm Res 356: 90–113

Gasparon M, Innocenti F, Manetti P, Peccerillo A, Tsegaye A (1993) Genesis of the Pliocene to Recent bimodal mafic–felsic volcanism in the Debre Zeyt area, central Ethiopia: volcanological and geochemical constraints. J Afr Earth Sci 17: 145–165

George R, Rogers N (1999) The petrogenesis of Plio–Pleistocene alkaline volcanic rocks from the Tosa Sucha region, Arba Minch, southern Main Ethiopian Rift. Acta Vulcanol 11: 121–130

Ghiorso MS, Gualda GAR (2015) An H_2O–CO_2 mixed fluid saturation model compatible with rhyolite-MELTS. Contrib Mineral Petrol 169: 1–30

Ghiorso MS, Sack RO (1995) Chemical mass transfer in magmatic processes IV. A revised and internally consistent thermodynamic model for the interpolation and extrapolation of liquid–solid equilibria in magmatic systems at elevated temperatures and pressures. Contrib Mineral Petrol 119: 197–212

Gualda GAR, Ghiorso MS, Lemons RV, Carley TL (2012) Rhyolite-MELTS: a modified calibration of MELTS optimized for silica-rich, fluid-bearing magmatic systems. J Petrol 53: 875–890

Hart SR (1984) A large-scale isotope anomaly in the Southern Hemisphere mantle. Nature 309: 753–757

Hart SR (1988) Heterogeneous mantle domains: signatures, genesis and mixing chronologies. Earth Planet Sci Lett 90: 273–296

Heinonen JS, Spera FJ, Bohrson WA (2022) Thermodynamic limits for assimilation of silicate crust in primitive magmas. Geology 50: 81–85

Hildreth W, Wilson CJ (2007) Compositional zoning of the Bishop Tuff. J Petrol 48: 951–999

Hunt JA, Mather TA, Pyle DM (2020) Morphological comparison of distributed volcanic fields in the Main Ethiopian Rift using high-resolution digital elevation models. J Volcanol Geotherm Res 393: 106732

Jacobsen SB, Wasserburg GJ (1980) Sm–Nd isotopic evolution of chondrites. Earth Planet Sci Lett 50: 139–155

Janoušek V, Farrow CM, Erban V (2006) Interpretation of whole-rock geochemical data in igneous geochemistry: introducing Geochemical Data Toolkit (GCDkit). J Petrol 47: 1255–1259

Janoušek V, Moyen JF, Martin H, Erban V, Farrow C (2016) Geochemical Modelling of Igneous Processes – Principles and Recipes in R Language. Bringing the Power of R to a Geochemical Community. Springer, Berlin, pp 1–346

Kereszturi G, Németh K, Cronin SJ, Procter J, Agustín-Flores J (2014) Influences on the variability of eruption sequences and style transitions in the Auckland Volcanic Field, New Zealand. J Volcanol Geotherm Res 286: 101–115

Kshirsagar P, Siebe C, Guilbaud MN, Salinas S (2016) Geological and environmental controls on the change of eruptive style (phreatomagmatic to Strombolian-effusive) of Late Pleistocene El Caracol tuff cone and its comparison with adjacent volcanoes around the Zacapu Basin (Michoacán, México). J Volcanol Geotherm Res 318: 114–133

Le Maitre RW, Streckeisen A, Zanettin B, Le Bas MJ, Bonin B, Bateman P, Bellieni G, Dudek A, Efremova S, Keller J, Lameyre J, Sabine PA, Schmid R, Sørensen H, Wooley AR (2002) Igneous Rocks. A Classification and Glossary of Terms. Recommendations of the International Union of Geological Sciences Subcommission on the Systematics of Igneous Rocks, 2nd Edition. Cambridge University Press, Cambridge–New York, pp 1–193

Leake BE, Woolley AR, Arps CE, Birch WD, Gilbert MC, Grice JD, Hawthorne FC, Kato A, Kisch HJ, Krivovichev VG, Linthout K, Laird J, Mandarino JA, Maresch WV, Nickel EH, Rock NMS, Schumacher JC, Smith DC, Stephenson NCN, Ungaretti L, Whittaker EJW, Youzhi G (1997) Nomenclature of amphiboles; report of the Subcommittee on Amphiboles of the International Mineralogical Association Commission on new minerals and mineral names. Canad Mineral 35: 219–246

Liew TC, Hofmann AW (1988) Precambrian crustal components, plutonic associations, plate environment of the Hercynian Fold Belt of Central Europe: indications from a Nd and Sr isotopic study. Contrib Mineral Petrol 98: 129–138

Martin-Jones CM, Lane CS, Pearce NJ, Smith VC, Lamb HF, Schaebitz F, Viehberg F, Brown MC, Frank U, Asrat A (2017) Recurrent explosive eruptions from a high-risk Main Ethiopian Rift volcano throughout the Holocene. Geology 45: 1127–1130

Megerssa L, Rapprich V, Novotný R, Verner K, Erban V, Legesse F, Manaye M (2019) Inventory of key geosites in the Butajira Volcanic Field: perspective for the first geopark in Ethiopia. Geoheritage 11: 1643–1653

Meshesha D, Shinjo R (2007) Crustal contamination and diversity of magma sources in the northwestern Ethiopian volcanic province. J Mineral Petrol Sci 102: 272–290

Míková J, Denková P (2007) Modified chromatographic separation scheme for Sr and Nd isotope analysis in geological silicate samples. J Geosci 52: 221–226

Milner DM, Cole JW, Wood CP (2003) Mamaku Ignimbrite: a caldera-forming ignimbrite erupted from a compositionally zoned magma chamber in Taupo Volcanic Zone, New Zealand. J Volcanol Geotherm Res 122: 243–264

Morimoto N (1988) Nomenclature of pyroxenes. Mineral Petrol 39: 55–76

Németh K, White JDL, Reay A, Martin U (2003) Compositional variation during monogenetic volcano growth and its implications for magma supply to continental volcanic fields. J Geol Soc, London 160: 523–530

Nobre Silva IG, Weis D, Barling J, Scoates J (2009) Leaching systematics and matrix elimination for the determination of high-precision Pb isotope compositions of ocean island basalts. Geochem Geophys Geosyst 10: Q08012, DOI 10.1029/2009GC002537

Pearce JA (1996) A user's guide to basalt discrimination diagrams. In: Wyman DA (ed) Trace Element Geochemistry of Volcanic Rocks: Applications for Massive Sulphide Exploration. Geological Association of Canada, Short Course Notes 12: 79–113

Peccerillo A, Barberio MR, Yirgu G, Ayalew D, Barbieri M, Wu TW (2003) Relationships between mafic and peralkaline silicic magmatism in continental rift settings: a petrological, geochemical and isotopic study of the Gedemsa Volcano, Central Ethiopian rift. J Petrol 44: 2003–2032

Pik R, Deniel C, Coulon C, Yirgu G, Hoffmann C, Ayalew D (1999) Isotopic and trace element signatures of Ethiopian flood basalts: evidence for plume–lithosphere interactions. Geochim Cosmochim Acta 63: 2263–2279

Pin C, Briot D, Bassin C, Poitrasson F (1994) Concomitant separation of strontium and samarium–neodymium for isotopic analysis in silicate samples, based on specific extraction chromatography. Anal Chim Acta 298: 209–217

Rapprich V, Žáček V, Verner K, Erban V, Goslar T, Bekele Y, Legesa F, Hroch T, Hejtmánková P (2016) Wendo Koshe Pumice: the latest Holocene silicic explosive eruption product of the Corbetti volcanic system (southern Ethiopia). J Volcanol Geotherm Res 310: 159–171

Rapprich V, Shields S, Halodová P, Lindline J, van Wyk de Vries B, Petronis MS, Valenta J (2017) Fingerprints of magma mingling processes within the Miocene Zebín tuff cone feeding system (Jičín Volcanic Field, Czech Republic). J Geosci 62: 215–229

Rehkämper M, Hofmann AW (1997) Recycled ocean crust and sediment in Indian Ocean MORB. Earth Planet Sci Lett 147: 93–106

Rochette P, Tamrat E, Féraud G, Pik R, Courtillot V, Ketefo E, Coulon C, Hoffmann C, Vandamme D, Yirgu G (1998) Magnetostratigraphy and timing of the Oligocene Ethiopian traps. Earth Planet Sci Lett 164: 497–510

Rooney TO (2010) Geochemical evidence of lithospheric thinning in the southern Main Ethiopian Rift. Lithos 117: 33–48

Rooney TO, Bastow ID, Keir D (2011) Insights into extensional processes during magma assisted rifting: evidence from aligned scoria cones. J Volcanol Geotherm Res 201: 83–96

Schilling JG, Kingsley RH, Hanan BB, McCully BL (1992) Nd–Sr–Pb isotopic variations along the Gulf of Aden: evidence for mantle plume–continental lithosphere interaction. J Geophys Res 97: 10927–10966

Schmincke HU (1977) Phreatomagmatische Phasen in quartären Vulkanen der Osteifel. Geol Jb 39: 3–45

Siegburg M, Gernon TM, Bull JM, Keir D, Barfod DN, Taylor RN, Abebe B, Ayele A (2018) Geological evolution of the Boset-Bericha Volcanic Complex, Main Ethiopian Rift: $^{40}Ar/^{39}Ar$ evidence for episodic Pleistocene to Holocene volcanism. J Volcanol Geotherm Res 351: 115–133

Steiger RH, Jäger E (1977) Subcommission on Geochronology: convention on the use of decay constants in geo- and cosmochronology. Earth Planet Sci Lett 36: 359–362

Stewart K, Rogers N (1996) Mantle plume and lithosphere contributions to basalts from southern Ethiopia. Earth Planet Sci Lett 139: 195–211

Sun SS, McDonough WF (1989) Chemical and isotopic systematics of oceanic basalts; implications for mantle composition and processes. In: Saunders AD, Norry MJ (eds) Magmatism in the Ocean Basins. Geological Society of London Special Publications 42: 313–345

Tanaka T, Togashi S, Kamioka H, Amakawa H, Kagami H, Hamamoto T, Yuhara M, Orihashi Y, Yoneda S, Shimizu H, Kunimaru T, Takahashi K, Yanagi T, Nakano T, Fujimaki H, Shinjo R, Asahara Y, Tanimizu M, Dragusanu C (2000) JNdi-1: a neodymium isotopic reference in consistency with LaJolla neodymium. Chem Geol 168: 279–281

Tracy RJ, Robinson P (1977) Zoned titanian augite in alkali olivine basalt from Tahiti and the nature of titanium substitution in augite. Amer Miner 62: 634–645

Trua T, Deniel C, Mazzuoli R (1999) Crustal control in the genesis of Plio-Quaternary bimodal magmatism of the Main Ethiopian Rift (MER): geochemical and isotopic (Sr, Nd, Pb) evidence. Chem Geol 155: 201–231

Verner K, Megerssa L, Hroch T, Buriánek D, Martínek K, Janderková J, Šíma J, Kryštofová E, Gebremariyam H, Tadesse E, Legesse F, Nisra E, Abateneh B, Assefa G, Valenta J, Pécskay Z, Hejtmánková P, Krejčí Z (2018) Explanatory notes to the thematic geoscientific maps of Ethiopia at a scale of 1 : 50 000, Map Sheet 0637-D3 Arba Minch. Czech Geological Survey, Prague

Vieten K, Hamm HM (1978) Additional notes On the calculation of the crystal chemical formula of clinopyroxenes and their contents of Fe^{3+} from microprobe analyses. Neu Jb Mineral, Mh 2: 71–83

Wasserburg GJ, Jacobsen SB, DePaolo DJ, McCulloch MT, Wen T (1981) Precise determination of Sm/Nd ratios, Sm and Nd isotopic abundances in standard solutions. Geochim Cosmochim Acta 45: 2311–2323

Zindler A, Hart SR (1986) Chemical geodynamics. Ann Rev Earth Planet Sci 14: 493–571

Žák J, Paterson SR, Janoušek V, Kabele P (2009) The Mammoth Peak sheeted complex, Tuolumne Batholith, Sierra Nevada, California: a record of initial growth or late thermal contraction in a magma chamber? Contrib Mineral Petrol 158: 447–470